Simultaneous design and operational optimization of hybrid CSP-PV plants

L.Pilotti[1], M.Colombari[1], A.F.Castelli[1], M.Binotti[1], A.Giaconia[2], E.Martelli[1*]

[1]Politecnico di Milano
[2]ENEA, Casaccia Research Center
* corresponding author email: emanuele.martelli@polimi.it

Abstract

The dispatchability of renewable power plants and the role of energy storage are gaining relevance leading to the development of hybrid CSP-PV plants. This work investigates the optimal design of highly integrated CSP-PV power plants. The integration occurs not only at grid level (synergic operation as a virtual power plant), but also through the introduction of electric heaters, placed in parallel to the solar field: the excess PV electricity is converted into heat by electric heaters and stored in the CSP hot storage tank. The whole system design is optimized devising an ad hoc Mixed Integer Linear Program (MILP) which co-optimizes design and operational variables with accurate linearization of all nonlinear effects. Compared to the respective stand-alone technologies (only CSP or PV plus battery), the results show that the hybrid solutions can achieve similar or better dispatchability levels at a lower cost of electricity (LCOE reduction between -30% and -50%).

Nomenclature

Acronyms	Description
BESS	Battery Energy Storage System
CSP	Concentrated Solar Power
CRF	Capital Recovery Factor
DNI	Direct Normal Irradiance
EH	Electric Heater
EMS	Energy Management System
EP	Extreme Period
ESS	Energy Storage System
FWH	Feedwater Heater
GCR	Ground Coverage Ratio
GHI	Global Horizontal Irradiance
HTF	Heat Transfer Fluid
LCOE	Levelized Cost of Electricity
LFR	Linear Fresnel Reflectors
MILP	Mixed-Integer Linear Programming
MS	Molten Salt
NOCT	Nominal Operating Cell Temperature
PB	Power Block
PV	Photovoltaic
PT	Parabolic Trough
SAM	System Advisor Model
SF	Solar Field
TAC	Total Annual Cost
TES	Thermal Energy Storage
TMY	Typical Meteorological Year
TP	Typical Period

VPP Virtual Power Plant

Variable	Description	Units
A^{PV}	PV active surface installed	$[m_2]$
A^{SF}	SF active surface installed	$[m_2]$
$\dot{Q}^{in}_{PB,max}$	PB nominal thermal input (i.e. size)	$[MW_t]$
E_{BESS}	BESS nominal capacity	$[MWh_e]$
E_{TES}	TES nominal capacity	$[MWh_t]$
$E^{hot}_{max}/E^{cold}_{max}$	Hot and cold tank maximum capacity	$[MWh_t]$
P_{EH}	EHs rated power	$[MW_e]$
z^{PB}_t	PB on/off status	[-]
$\delta^{PB}_{on,t}$	PB start-up binary variable	[-]
$\delta^{PB}_{off,t}$	PB shut-down binary variable	[-]
$\dot{H}^{in}_{PB,t}$	PB thermal power input	$[MW_t]$
$\dot{H}^{out}_{PB,t}$	Enthalpic content of the MS exiting the PB	$[MW_t]$
$P^{PB}_{out,t}$	PB electric power output	$[MW_e]$
$P^{PV}_{out,t}$	PV electric power output	$[MW_e]$
$\dot{Q}^{SF}_{out,t}$	Thermal power output from SF	$[MW_t]$
$P^{BESS}_{ch,t}$	BESS charging power	$[MW_e]$
$P^{BESS}_{disch,t}$	BESS discharging power	$[MW_e]$
SOC^{BESS}_t	BESS State-of-Charge (SoC)	$[MWh_e]$
U^{hot}_t/U^{cold}_t	Hot and cold tank energy storage levels	$[MWh_t]$
$\dot{H}^{in}_{SF,t}$	SF input thermal power	$[MW_t]$
$\dot{H}^{wk}_{SF,t}$	Thermal power from SF for cold tank warm-keeping	$[MW_t]$
$\dot{H}^{hot}_{toPB,t}$	Thermal power from hot tank to PB	$[MW_t]$
$\dot{H}^{hot}_{tocold,t}$	Thermal power from hot to cold tank	$[MW_t]$
$\dot{Q}^{hot}_{EH,t}$	Thermal power generated via the EH and stored in the hot tank	$[MW_t]$
$\dot{Q}^{cold}_{EH,t}$	Thermal power generated via the EH and stored in the cold tank	$[MW_t]$
P^{grid}_t	Electrical power exported from the plant to the grid	$[MW_e]$

Parameter	Description	Units
$\hat{P}^{PV,spec.}_t$	Hourly specific electricity production from the PV field	$[\frac{MW_e}{m^2}]$
$\hat{Q}^{SF,spec.}_t$	Hourly specific thermal energy production per SF field loop	$[\frac{MW_t}{loop}]$
$\hat{P}^{SF,spec}_{pumps,t}$	Hourly specific electricity consumptions of SF pumps per loop	$[\frac{kW_e}{loop}]$
$\hat{k}_1, \hat{k}_2, \hat{k}_3$	Linearization coefficients of the PB performance map	$[\frac{MW_e}{MW_t}]$, $[\frac{MW_e}{MW_t}]$, $[MW_e]$
$\hat{w}_1, \hat{w}_2, \hat{w}_3$	Linearization coefficients of the heat losses correlations in the two tanks of the TES	$[\frac{kW_{th}}{kWh_{th}}]$, $[\frac{kW_{th}}{kWh_{th}}]$, $[kW_{th}]$
$\hat{T}_{amb}$	Ambient temperature	$[K]$
$\hat{T}_{ref}$	Reference temperature	$[K]$
$\hat{Y}_{1,j}, \hat{Y}_{2,j}$	Linearization coefficients of the correlation for the residual enthalpic content of MS coming from PB heat exchanger	$[\frac{MW_e}{MW_t}]$, $[\frac{MW_e}{MW_t}]$
$\hat{c}^{mean}_{p,MS}$	MS specific heat capacity at constant pressure	$[\frac{kJ}{kg \cdot K}]$
$\hat{c}^{mean}_{v,MS}$	MS specific heat capacity at constant volume	$[\frac{kJ}{kg \cdot K}]$
$\hat{R}^{lim}_{up}$	Ramp-up limit related to PB load variation	$[MW_e]$
$\hat{R}^{lim}_{down}$	Ramp-down limit related to PB load variation	$[MW_e]$

$\hat{\eta}_{ch}^{BESS}$	BESS charge efficiency	[-]
$\hat{\eta}_{disch}^{BESS}$	BESS discharge efficiency	[-]
$\hat{C}_{rate}^{BESS}$	BESS maximum c-rate	$[\frac{MWh_e}{MW_e}]$
$\hat{\eta}_{EH}$	EH conversion efficiency	[-]
$\hat{A}_{tot}$	Total active surface of land area available	$[m^2]$
$\hat{p}_d$	Fraction of annual demand to be satisfied	[-]
$\hat{D}_t$	Hourly electricity demand	$[MW_e]$

1 Introduction

The decarbonization of the energy sector and the rapid deployment of power plants based on intermittent renewable energy sources will represent a key challenge in the next decades. Although PV and wind technologies have undergone rapid growth in the last years [1], intermittent electricity production represents a limit for their future development as stand-alone technologies. In addition to the cost of electricity and specific investment cost, today is fundamental to consider also other types of key performance indicators to assess plants and technologies dispatchability. A possible way to measure a power plant's dispatchability is to evaluate its ability to follow a target of load. Therefore dispatchability requires good plant controllability and operational flexibility (low minimum load, fast ramp-up/down, short start-up time). Even if not economically rewarded by current market mechanisms, the added value of dispatchability is already acknowledged by energy regulators since providing dispatchable renewable power will be essential for a carbon-neutral electric grid.

Most of the renewable technologies today available on the market, as Photovoltaic (PV), wind turbines and Concentrated Solar Power (CSP) are not dispatchable themselves and they are often equipped with Energy Storage Systems (ESS). For instance, batteries are used to improve the dispatchability of PV while Thermal Energy Storages (TES) are used for CSP plants. However, both technologies are highly capital intensive: the current cost of Battery Energy Storage Systems (BESS) makes the dispatchable PV (PV+ BESS) not economically competitive in the electricity market [2], while the complexity and cost of CSP components (solar field, steam cycle, primary heat exchanger and the thermal storage) makes it uneconomic without incentives [3].

A promising alternative being studied recently is integrating the PV and CSP technology, creating a hybrid solar-based power plant. The hybridization of CSP-PV technologies could be achieved according to different integration levels [4][5][6]:

- **Grid-level integration**: the two separate plants are virtually aggregated as a single entity at the grid connection point, but no physical energy transfer between the main components of the two technologies takes place (VPP concept [7]). The integration occurs only via the Energy Management System (EMS) that manages and controls the interactions between subsystems according to the variation in forecast of weather conditions and electricity demand. Such concept allows to delocalize the PV site and often represents the best solution to apply the hybrid concept in geographical locations where finding a large amount of continuous land may be problematic (e.g. Italy).
- **Technology-level integration**: hybrid plants integrated at the technological level are able to exchange energy between the respective system components. The transfer of energy from the PV plant to the CSP plant can take place in several ways:
  (i) **auxiliaries' integration**: the PV section can supply electricity for the auxiliaries of the CSP section [8];
  (ii) **power-to-heat integration** the PV section can supply electricity to run either Electric Heaters (EH) [6] or heat pumps [5] to generate heat for the CSP storage system. With

this set-up, thanks to the deeper integration level, the EMS can identify better operational strategies by exploiting the larger number of degrees of freedom available, compared to lower-integrated configurations;

- **Compact/advanced integration:** different parts of the solar spectrum are used to run the PV and CSP sections as done in the PV topping or spectral beam splitting concept [9].

As far as grid-level integrated CSP-PV are concerned, Cocco et al. [10] explored two different management strategies between the solar technologies assuming constant daily power output curves. From the comparative study, an improvement in the total energy production has been observed in case of a higher level of integration. Although the effectiveness of the grid-level hybridization was demonstrated for baseload plant operation, considerations regarding the economil advantage of the integration were not reported in the analysis. Starke et al. [11] compared different CSP-PV layouts, based on the solar tower and Parabolic Trough (PT). The work considers a plant located inChile and it uses a multi-objective optimization approach based on a genetic algorithm with four main design optimization variables: Solar Field (SF) size, TES size, PV tilt angle and power ratio, defined as the fraction between PV and CSP installed capacity). The Pareto front shows a clear trade-off between the capacity factor (CF) and the Levelized Cost Of Electricity (LCOE) of the plant. With respect to the stand-alone CSP configuration, the hybrid plant achieves higher CF (88% against 80% for the parabolic trough, 94% against 86% for the power tower) for the same levels of LCOE. Examples of existing grid-level hybrid CSP-PV plants are the recently-built Cerro Dominador in northern Chile [12], the Ottana CSP-CPV pilot facility [8] and the Partanna plant [13], both located in Italy, respectively in Sardinia and Sicily.

More recently, several studies investigated the CSP-PV hybridization occurring at the technology level. Most of them proposed the use of EH to store the excess PV in the TES of the CSP plant. Riffelmann et al. [14] have explored three scenarios corresponding to different integration levels of a CSP application based on Molten Salts (MS) as Heat Transfer Fluid (HTF). According to the study, the hybrid plant featuring the lowest LCOE is the one employing EH to charge the TES during daytime with the excess energy coming from the PV field. Gedle et al. in [15] compared two PT oil-based hybrid plants in Morocco, with and without EHs as HTF temperature boosters, obtaining an electricity cost 20% lower in the first option. Despite being a relatively cheap way to convert PV electricity into valuable heat for the TES, EHs show high exergy losses and poor conversion efficiency with respect to other conversion technologies (e.g. heat pumps). Therefore, the integration with higher performance energy devices such heat pumps has been studied as well. Mahdi et al. [5] recently researched the possibility of coupling High Temperature Heat Pumps (HTHPs) in a PT oil-based CSP-PV plant to reach 565°C in the TES hot tank. To target this temperature value, a HTHP system based on Brayton cycle should be adopted, a technology that currently is still not available on the market and may result in a more expensive and less reliable solution with respect to EHs.

A further step in the technical integration between the two solar technologies could be represented by the development of the compact CSP-PV concept. Rather than converting the excess electricity produced by the PV into heat, this hybrid setup allows to exploit directly the heat of the solar radiation not absorbed by the PV cells using a PV-topping (where the solar cells work simultaneously as the thermal receiver and PV converter) or spectral beam splitting (where solar radiation is spectrally separated to increase cells conversion efficiency and the below bandgap radiation is redirected to the thermal receiver of the CSP) systems. In this regard, Ju et al. [16] presented an extensive review of the technologies under development for CSP-PV compact systems, showing their advantages in terms of overall generating efficiency. However, these proposals involve several technical challenges and no projects or prototypes of this hybrid concept were reported at the time the article was published.

Nowadays, few practical examples of CSP-PV plants already in operation could be found and most of them still are under construction, such as the Redstone power plant (100 MW) in South Africa and the record-breaking Noor Energy 1 (1300 MW) in Dubai, equipped with the world's largest solar tower. The only two commercial operating CSP-PV power plants are the Cerro Dominador (110 MW CSP, 100 MW PV) in Chile [12] and the Partanna plant (4.3 MW CSP, 5.6 MW PV) in Sicily [13],

developed in collaboration with ENEA. Another CSP-PV pilot plant has been installed in Ottana (Sardinia) [8], featuring respectively 630 kW and 400 kW nominal power of the CSP and PV subsystems. The Ottana facility also includes a 430 kWh Sodium-Nickel battery bank for short-term energy storage. All the abovementioned plants are existing examples of grid-level integration, thus the PV and CSP sections are operated together, but they cannot physically interact with one another. To the author's knowledge, the commissioned Noor Midelt in Morocco, scheduled to start operation in 2022, is currently the sole practical example of a CSP-PV plant integrated also at technology-level, featuring an electrically heated e-TES [17].

The present work is part of the collaboration between the Politecnico di Milano and ENEA, which for many years has been active in developing CSP-based projects in southern Italy [13][18] and, in general, in the Mediterranean regions. We investigate the optimal design of hybrid CSP-PV plants which are technology and grid-level integrated**.** Even though virtual aggregation is not a common practice today for large power plants, several works have shown possible advantages deriving from the aggregation of production units [19][20]. Therefore we have taken a near future market perspective assuming that the regulation will allow also large VPPs to operate jointly in the energy market. Regarding the physical integration, we consider that the electricity of the PV system can be exploited to heat up part of the HTF subsequently stored in the hot tank of the CSP. The CSP plant uses MS as HTF and a steam Rankine cycle as Power Block (PB). Since the optimal design of the hybrid system design variables (size of the SF, PV, TES, PB) strongly depends on the operation of the system and desired dispatchability level, this work proposes a specific Mixed Integer Linear Programming (MILP) model for the co-optimization of hybrid system design and operation. Detailed non-linear models of each plant subsystem (PB, TES, PV, SF) have been developed and then linearized with ad hoc techniques. The MILP has been applied to determine the optimal hybrid system design for different levels of dispatchability.

The originality and the novelty of this work can be summarized in the following points:

- A novel, rigorous and replicable methodology for the design optimization of hybrid plants is proposed. The approach can be applied, with minor modifications, also to the different plant layouts, locations and technologies (e.g. CSP based on PT with thermal oil) for the preliminary performance design of hybrid plants.
- An innovative CSP layout based on the LFR technology and MS as HTF is investigated, as a promising alternative to standard CSP plants in small scale applications, such as island and EU-constrained locations where the land availability is limited.
- Different plant integration levels have been explored (i.e. grid and technology integration) to show the benefits deriving from the possible integration options between the two solar technologies.

2 Hybrid plant scheme

The hybrid plant considered in the study is shown in Figure 1. It is constituted by a PV field, a Battery Energy Storage System (BESS), a SF with concentrating solar collectors, a TES and a PB section. The PV plant is constituted by fixed-tilt PV panels with multi-crystalline silicon cells while the SF employs Linear Fresnel Reflectors (LFR) with MS as HTF and a direct two-tanks TES.

MS have been selected as HTF because they are not hazardous or inflammable and allow reaching higher temperatures than synthetic oil [21], with consequently better thermodynamic conversion efficiencies. LFR is preferred to other technologies such as the solar tower or PT for its compactness (i.e. higher ground coverage ratio) that results in limited land requirements. LFR technology, even if

characterized by lower optical efficiencies [22][23], represents a cheaper solution than PT and has potential advantages over PT especially when MS are used [24]: the LFR receiver is still above the mirrors not requiring rotating joints, thus reducing heat losses and risks related to MS solidification and allows for easier drainage of the SF (as a consequence of the continuous and long absorber pipes without low points in the circuit). The choice of LRF using MS for the CSP solar field has been made also to be consistent with the technological solution already adopted in the recently built Partanna plant [13] in Sicily (Italy).

In LFR systems, as in conventional CSP plants, the solar radiation is concentrated by means of solar collectors onto a receiver where the heat is removed using a HTF. During nominal plant operation, solar salts enter the SF at 290°C and exit at a temperature of 550°C. The thermal power collected by the SF is then converted into electricity by a conventional steam Rankine cycle in the PB section of the CSP plant. A EH provides a physical connection between the two systems and it is able to generate additional heat with the excess electric production of the PV field. According to the proposed layout, the electricity generated by the PV can be also stored in the BESS or fed directly into the grid.

As shown in the layout of Figure 1, hot MS exiting from the SF can be directly stored inside the TES hot tank or recirculated back to the cold tank, during the night for SF warm-keeping. The EH is placed in parallel to the SF, to heat-up part of the HTF and provides extra charge to the hot TES. Part of the HTF heated with the EH can be recirculated back to the cold tank, if necessary. Furthermore, a bypass linking the hot and cold tanks has been added to the plant layout in order to control the cold tank temperature and avoid problems related to MS solidification inside the tank. As a further safety measure, an electric tracing system present in the cold tank can intervene when simple MS mixing and circulation from the hot tank is not sufficient.

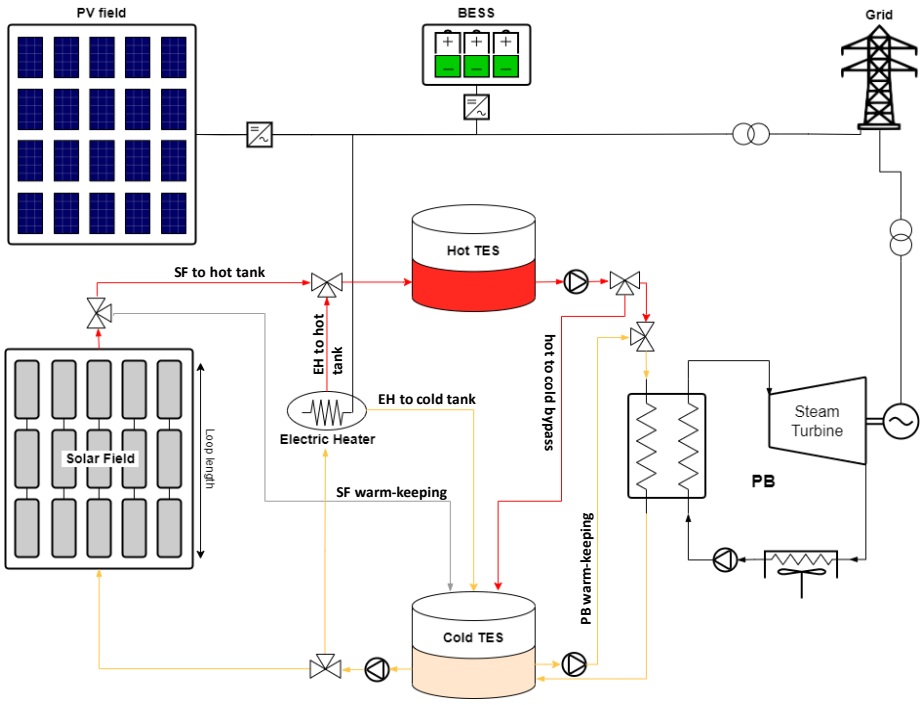

Figure 1 - Hybrid PV-CSP layout

During nominal operation, the bypass is closed and the hot salts are delivered to the power block heat exchangers train to provide the thermal input to the power cycle. The temperature and therefore the enthalpic content of the MS exiting the heat exchangers and entering the cold tank varies as function of the PB load: in particular, at very low PB loads, the outlet temperature of the salts might be much lower than the nominal value (290°C) and potential freezing issues may occur inside the

cold tank and the steam generator. For this reason, under particular operating conditions, may be necessary to increase the cold tank temperature via MS recirculation from the hot tank or via the energy generated by means of the EHs. Finally, when the PB is off, part of the MS in the cold TES are recirculated through the PB heat exchanger to perform the warm-keeping and avoid any solidification issues in the power section.

Priolo Gargallo (Sicily, Latitude 37.13° North, Longitude 15.21° East) has been chosen as a suitable location for the hybrid plant object of the study. The Typical Meteorological Year (TMY) file containing the weather data, provided by ENEA, features integral annual values of the Global Horizontal Irradiance (GHI) and Direct Normal Irradiance (DNI) of 1730 kWh/m^2/y and 1847 kWh/m^2/y, respectively with a mean external temperature of 17.6°C. A nominal DNI of 850 W/m^2 has been selected for the SF design, while a maximum of 150 hectares of contiguous land have been assumed to be available at the selected location, which is a typical value of the Italian context [18].

The hybrid plant is assumed to operate in the electricity market as a Virtual Power Plant (VPP), allowing the possibility of aggregating PV fields which are geographically close to the CSP plant but not located on the same site. Since dispatchability is one the key requirements for these plants (especially for the near-future, when fossil-fired dispatchable units will be phased out), we consider that the VPP has to meet (as far as possible) a variable electricity load (see) that features the same hourly trend as the Italian national demand curve (reference year 2019) [25] re-scaled with a peak of 50 MW.

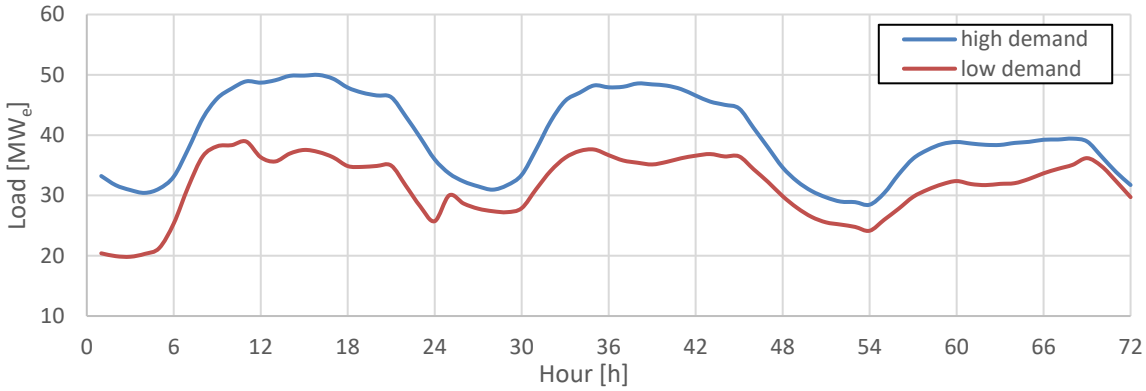

Figure 2 - Example of three consecutive days with high and low electricity demand of the variable load considered

The demand peak has been selected in agreement with the assumed land availability limit to install the solar field (150 hectares of active surface). Since no back-up unit (e.g., natural gas boiler) has been included in the plant layout, it is not possible to cover the entire demand throughout the year, especially during long periods with very low irradiance. However, we have followed a methodology that allows us to impose the minimum fraction of the electric load to be covered by the plant, defined as a percentage of the integral annual value of the demand (i.e. 50%, 60% of the total). Therefore the system and its components are sized accordingly, in order to meet the required fraction of demand (see also constraint (37) in Section 5.3).

3 Methodology

The schematic representation of the methodology adopted to model and optimize the design of the hybrid plant is shown in Figure 3. PV and SF components have been modeled with the System Advisor Model (SAM) [26], a widely adopted and proven open source software for modeling renewable generation systems: considering the weather data for the selected location, the specific

thermal power and electricity production have been estimated for the SF and PV, respectively (as described in Sections 4.1 and 4.2). The obtained results have been normalized for square meter of active surface (i.e. reflective area excluding space between mirrors) of LFR and PV panels. These normalized profiles have been clustered to identify a set of typical operating periods to be included in the MILP optimization model (Sections 5.2 and 5.3).

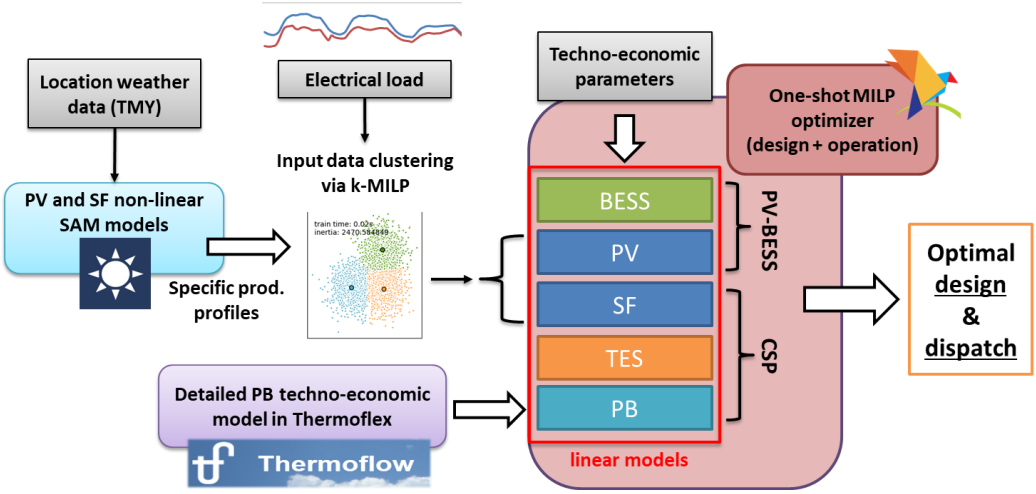

Figure 3 – Flowchart of the design-operation optimization algorithm

A detailed model of the PB component, constituted of a re-heated steam Rankine cycle, has been developed with the plant simulation software Thermoflex [27]. The thermodynamic cycle design has been performed for different net power output and for each design the part-load performance and the impact of the ambient temperature on cycle efficiency have been assessed. The obtained results have been used to derive cost and performance size dependent correlations subsequently linearized and included in the MILP optimization model (see Section 4.3). The normalized PV and SF fields production profiles for the typical periods and the linearized cost and performance curves of the subsystems are included in the MILP framework and used to optimize the hybrid system design. The MILP optimizes simultaneously the size and the operation of each subsystem (across the typical periods) with the objective of minimizing the Total Annual Cost (TAC), which is the sum of annualized capital and operating costs of the system. Further details are reported in Section 5.

It is important to note that the MILP optimization model can be easily extended to CSP plants employing different technologies for the solar field (e.g., solar tower) and power block (e.g., organic Rankine cycles, supercritical CO_2 cycles).

4 Sub-systems modeling

4.1 PV field

For the PV field, the multi-crystalline silicon technology and a fixed panel orientation have been adopted, while a lithium-ion BESS has been selected as stationary electricity storage. The parameters used to characterize the PV panel and the battery storage are reported in Table 1. The data in Table 1 refer to the SunPower SPR-P17-350-COM PV module available in the SAM database [26]. The design values of tilt angle and the Ground Coverage Ratio (GCR) of the PV are not independent: indeed, each GCR corresponds to a determined optimum tilt angle that maximizes the PV yearly generation. This is due to the self-shading occurring between the rows of the array, especially for low solar altitudes. Tighter module rows, corresponding to high GCR values, are more penalized by self-shading effects than looser ones. Hence, the adoption of higher GCR results in

lower tilt angle optimal values, because the incoming radiation from low sun position cannot be exploited effectively.

Table 1 – PV and BESS technical parameters

PV module	**SunPower SPR-P17-350-COM** [28]
Technology	Multi-crystallin silicon
Module width	0.998 m
Module length	2.067 m
Tilt/Azimuth angle	24°/180°
GCR	0.5
Nominal cell efficiency	17.14%
Power temperature coefficient	-0.415%
Heat exchange coefficient @ NOCT conditions	0.6
Total system losses (mismatch, electrical, wiring, nameplate)	5.5%
Soiling losses	5%
Yearly power derating	0.06%/y
Inverter	
DC to AC power ratio	1.25
Inverter efficiency	96%
BESS	
Technology	Lithium-ion
Charge/discharge efficiency	97%/97%
C-rate	1 MW/MWh

A simplified sensitivity analysis on GCR values has been carried out, considering self-shading losses only, without taking into account the influence of any physical obstacle. The azimuth angle has been set to 180° (i.e. facing South) for all cases, while the optimal tilt for the selected site is obtained for each GCR. Results are reported in Table 2: comparing the trend of the specific annual generation with the self-shading losses and considering also the strict requirement on the maximum contiguous land available, a tradeoff value of 0.5 has been selected as GCR (optimal tilt of 24°) for the PV field design.

Table 2 - Self-shading loss and specific yearly generation for different values of the optimal GCR and tilt angle

GCR	**0.01**	**0.3**	**0.4**	**0.5**	**0.6**
Tilt angle	**29°**	**27°**	**26°**	**24°**	**19°**
Power specific annual generation $[\frac{kWh}{kW \cdot y}]$	1432	1421	1415	1405	1388
Area specific annual generation $[\frac{kWh}{m^2 \cdot y}]$	2	73	97	120	143
Self-shading loss [-]	0.0%	0.8%	1.2%	1.9%	3.1%

Once all design parameters are defined (Table 2), the expected PV production profile can be derived from the TMY of the case study location. The specific PV generation is estimated with a detailed PV model obtained with SAM [26], taking into account the effect of outside temperature, wind speed, shading and all the system losses. The specific PV output curve ($\hat{P}_t^{PV,spec.}$) for each hour of the TMY is shown in Figure 4.

$$P_{out,t}^{PV} \leq A^{PV} \cdot \hat{P}_t^{PV,spec.} \qquad \forall t \in T \qquad (1)$$

Thanks to Eq. (1) then is possible to correlate the installed area (A^{PV}) with the instantaneous power output of PV field ($P_{out,t}^{PV}$) through its specific generation profile ($\hat{P}_t^{PV,spec.}$), where the "≤" sign accounts for the possibility of PV curtailment.

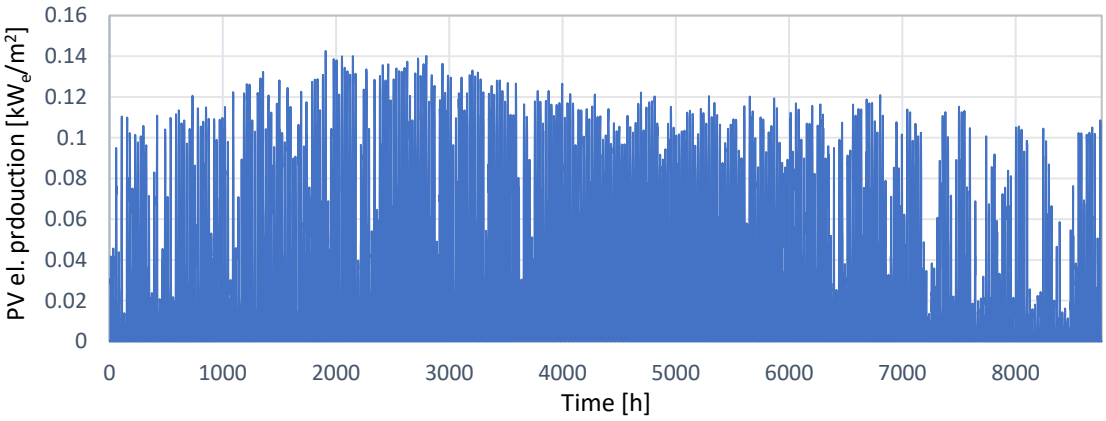

Figure 4 - Specific PV power generation profile

4.2 Solar Field

The CSP field is based on a LFR technology working with molten salts as HTF and with a direct two tanks TES. The SF modules are constituted of FRENELL collectors [29] with HCEMS-11 as receiver tubes [30], developed by the Italian company Archimede [31], whose main characteristics are reported in Table 3. A loop length of 771 m (the same as the Partanna plant [13]) has been considered for the SF design. To account for the optical efficiency variation with the sun position, two Incidence Angle Modifiers (IAM) function of the longitudinal (θ_i) and transversal ($\theta_\perp$) incidence angles on the Fresnel collector are used. The off-design collector optical efficiency is thus computed with Eq. (2):

$$\eta_{opt}(\theta_z,\gamma) = \eta_{opt,des} \cdot IAM(\theta_z,\gamma) \approx \eta_{opt,des} \cdot IAM(\theta_i) \cdot IAM(\theta_\perp) \quad (2)$$

The values of $IAM(\theta_i)$ and $IAM(\theta_\perp)$ for the FRENELL collector are taken from the Thermoflex database [27]. The correlation in Eq. (3) for the estimation of receiver tube thermal losses per unit length with HTF temperature variation is derived from experimental and theoretical data obtained by ENEA [32]:

$$\dot{Q}_{th}^{loss}[W/m] = 1.63 \cdot 10^{-5} \cdot T^3[°C] - 0.013 \cdot T^2[°C] + 4.38 \cdot T[°C] - 504.13 \quad (3)$$

IAM values for different incidence angles and thermal losses per unit length are shown in Figure 5.

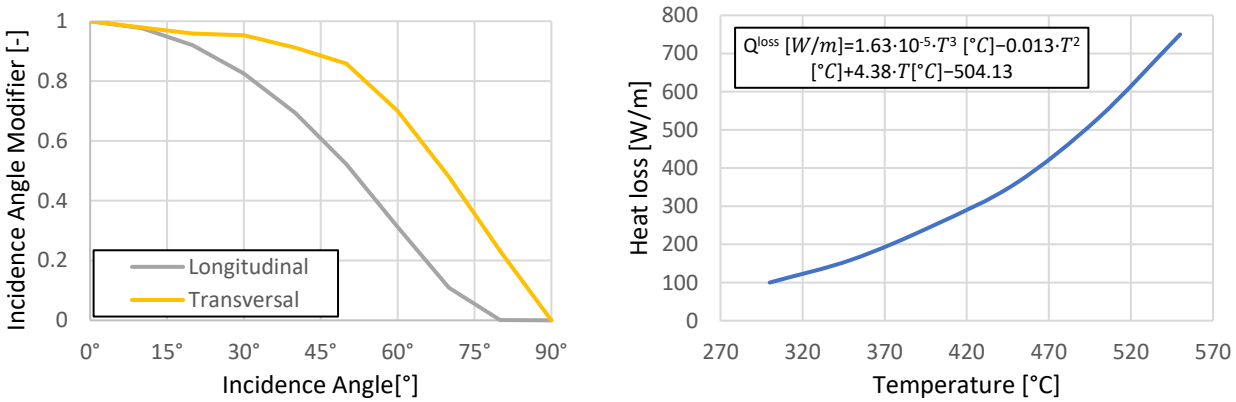

(a) (b)

Figure 5 – (a) IAM as function of the longitudinal and transversal incidence angle and (b) thermal losses per unit length as function of the receiver tube temperature

The above-mentioned correlations for the LFR optical and thermal efficiencies are implemented in a SAM model, where a large solar field is designed (400 MW_{th}). Pressure drops and thermal losses in the piping system are computed assuming default values for the maximum/minimum HTF velocity in the headers (2/3 m/s). Starting from the hourly values of the DNI of the TMY, it is then possible to evaluate the specific heat generated from each loop of the SF for each hour of the year (Figure 6a). Other than the heat absorbed by the HTF, also the mass flow rate circulating in the single SF loop, the HTF temperature at the outlet of the SF for any irradiance condition and the specific power consumption of SF pumps per loop (Figure 6b) have been obtained.

Table 3 - Main geometrical data and performances of the linear Fresnel collector and receiver

Collector	**FRENELL** [29]
Number of mirrors in a module (#)	16
Module length (m)	44.8
Module width (m)	12
Focal length (m)	7.4
Nominal optical efficiency (%)	64.7
Receiver	**HCEMS-11** [30]
External receiver tube diameter (mm)	70
Receiver thickness (mm)	3
Transmittance (-)	0.966
Absorbance (-)	0.95
Emissivity (-)	0.0595+2.61E-07*T^2 [°C]
Thermal loss at design conditions (W/m)	255 @ 400°C, 730 @ 550°C

Eq. (4) expresses the relationship between the installed number of loops (N_{loop}^{SF}) and the instantaneous thermal production ($\dot{Q}_{out,t}^{SF}$), via the SF specific thermal generation profile ($\hat{Q}_t^{SF,spec.}$). Note that Eq. (4) allows for partial SF defocusing by imposing only an upper limit on SF generation. Finally, Eq. (5) is used to derive the hourly power consumption of SF pumps ($P_{pumps,t}^{SF}$), computed as the electricity consumption of the SF pumps specific to loop of SF ($\hat{P}_{pumps,t}^{SF,spec}$) multiplied by the number of SF loops (N_{loop}^{SF}).

$$\dot{Q}_{out,t}^{SF} \leq N_{loop}^{SF} \cdot \hat{Q}_t^{SF,spec.} \qquad \forall t \in T \quad (4)$$

$$P^{SF}_{pumps,t} = N^{SF}_{loop} \cdot \hat{P}^{SF,spec}_{pumps,t} \qquad \forall t \in T \qquad (5)$$

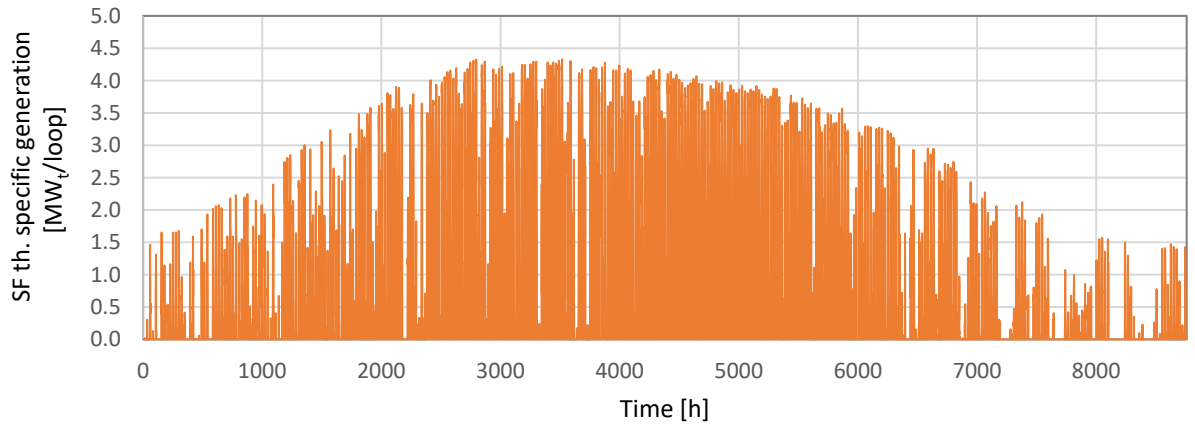

(a)

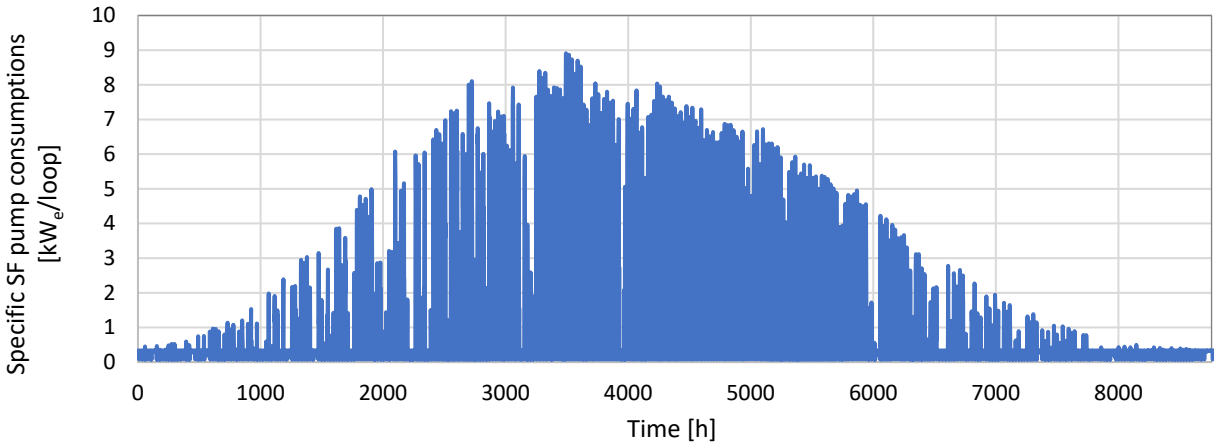

(b)

Figure 6 - Specific SF thermal power production (a) and specific pumps electricity consumption (b)

4.3 Power block

The power section of the CSP field is based on a conventional steam Rankine cycle with reheat, featuring three low and three high pressure feedwater heaters (FWH). The plant layout designed in Thermoflex is reported in Figure 7, while the main design assumptions are specified in Table 4.

The adopted steam cycle configuration is taken from our previous work [33], where different part-load strategies were discussed. In particular, in [33], we found that the best strategy is to adopt a turbine re-admission valve (valve V2 in Figure 7). From 100% to 60%, the steam cycle is controlled in sliding pressure, then for lower loads valve V2 is progressively closed in order to keep high the pressure of the steam bleed sent to the high pressure feedwater preheater. By doing so, feedwater is preheated to a temperature sufficient to guarantee a skin temperature of the economizer tubes above 245°C in the load range 60%-30%.

Finally, as detailed in [33], for each value of MS mass flow rate and ambient temperature, the rotational speed of the air-cooled condenser fans has been optimized to maximize the PB net efficiency.

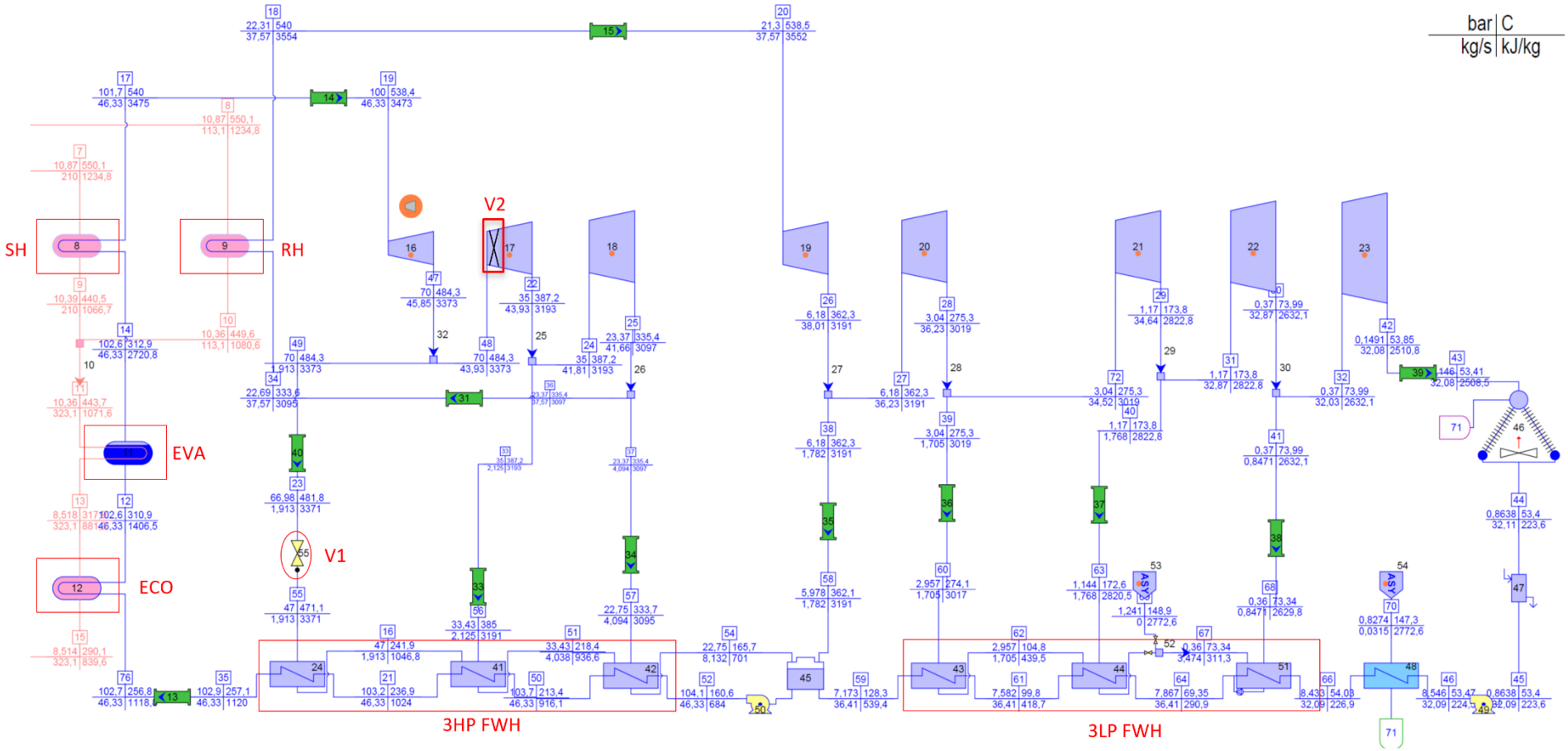

Figure 7 – Layout of the re-heated steam Rankine cycle implemented in Thermoflex

The preliminary design, capital cost and off-design operating conditions have been computed with Thermoflex [27], one of the reference software for modeling steam cycles [34]. The part-load efficiency map has been determined for different PB sizes in order to determine the influence of both size and part-load on the PB efficiency.

Table 4 - Main assumption and design parameters of the steam Rankine cycle.

Parameter	Assumptions
Net power [MW_e]	10-100
Maximum HTF temperature [°C]	550
Minimum HTF temperature [°C]	290
Steam temperature at SH/RH outlet [°C]	540/540
Steam pressure at SH/RH outlet [bar]	100/21
ΔT pinch at EVA [°C]	5
ΔT subcooling at EVA [°C]	5
ΔT pinch condenser [°C]	7
Condensing pressure [bar]	0.145
Net cycle efficiency [%]	39-41*
*depending on PB size	

The nonlinear map computed with Thermoflex is shown in Figure 9. Such map has been linearized using the approach proposed by Yokoyama [35] and extended by Zatti et al. [36] and Gabrielli et al. [37]. The idea is to linearize directly the correlation between the output power and inlet thermal power $\dot{Q}^{in}_{PB,t}$ (which is related to the load) and size $\dot{Q}^{in}_{PB,max}$, as reported in Eq. (6):

$$P^{out}_t = \left(\hat{k}_1 \cdot \dot{Q}^{in}_{PB,t} + \hat{k}_2 \cdot \dot{Q}^{in}_{PB,max} + \hat{k}_3 \cdot z^{PB}_t\right) \cdot \hat{f}(T_{amb}) \qquad \forall t \in T \qquad (6)$$

$$\hat{f}(T_{amb}) = -6.4873 \cdot 10^{-5} \cdot \hat{T}^2_{amb} + 3.6278 \cdot 10^{-2} \cdot \hat{T}_{amb} - 4.0369 \qquad (7)$$

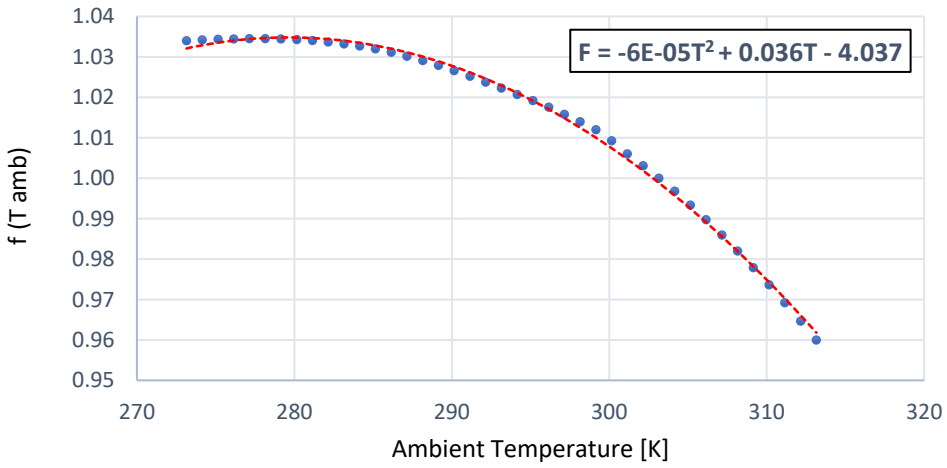

Figure 8 – PB performances correction factor as function of the ambient temperature

The coefficient $\hat{f}(T_{amb})$ is a correction parameter used to account the effect of the ambient temperature on the power output. The correlation between coefficient $\hat{f}$ and the ambient temperature in Eq. (7) has been derived assuming a design ambient temperature of 30°C (303.15 K).

Dividing Eq. (6) by the thermal power $\dot{Q}_{PB,t}^{in}$, we obtain the expression of the efficiency in Eq. (8), which is the sum of three contributions: a constant term ($\hat{k}_1$), a term dependent on the incoming thermal input fraction ($\hat{k}_2 \cdot \frac{\dot{Q}_{PB,max}^{in}}{\dot{Q}_{PB,t}^{in}}$) which takes into account the variation in efficiency under part-load conditions, and a third term ($\frac{\hat{k}_3}{\dot{Q}_{PB,t}^{in}}$) which takes into account the size effect. In general, the coefficient $\hat{k}_3$ is zero for technologies with no effect of size on efficiency (e.g., modular components such as fuel cells, batteries), while it is negative for technologies with beneficial size effects on efficiency (such as steam cycles or gas turbines).

$$\eta_t^{el} = \frac{P_t^{out}}{\dot{Q}_{PB,t}^{in}} = \left(\hat{k}_1 + \hat{k}_2 \cdot \frac{\dot{Q}_{PB,max}^{in}}{\dot{Q}_{PB,t}^{in}} + \frac{\hat{k}_3}{\dot{Q}_{PB,t}^{in}}\right) \cdot \hat{f}(T_{amb}) \qquad \forall t \in T \quad (8)$$

The three coefficients have been determined by best-fitting the linear relation over the nonlinear map for a set of points at different sizes and loads. In Table 5 the values of the coefficients fitting two different PB size ranges are reported.

Table 5 – PB performance map coefficients for different size ranges

Coefficient	$\hat{k}_1$ $[MW_e/MW_{th}]$	$\hat{k}_2$ $[MW_e/MW_{th}]$	$\hat{k}_3$ $[MW_e]$
20-50 $[MW_e]$	0.4258	-0.0226	-0.7163
50-100 $[MW_e]$	0.4335	-0.0291	-0.5217

Figure 9 shows the comparison between the data obtained with Thermoflex and the approximated values calculated with Eq. (6) and (8) for different PB load ranges and sizes.

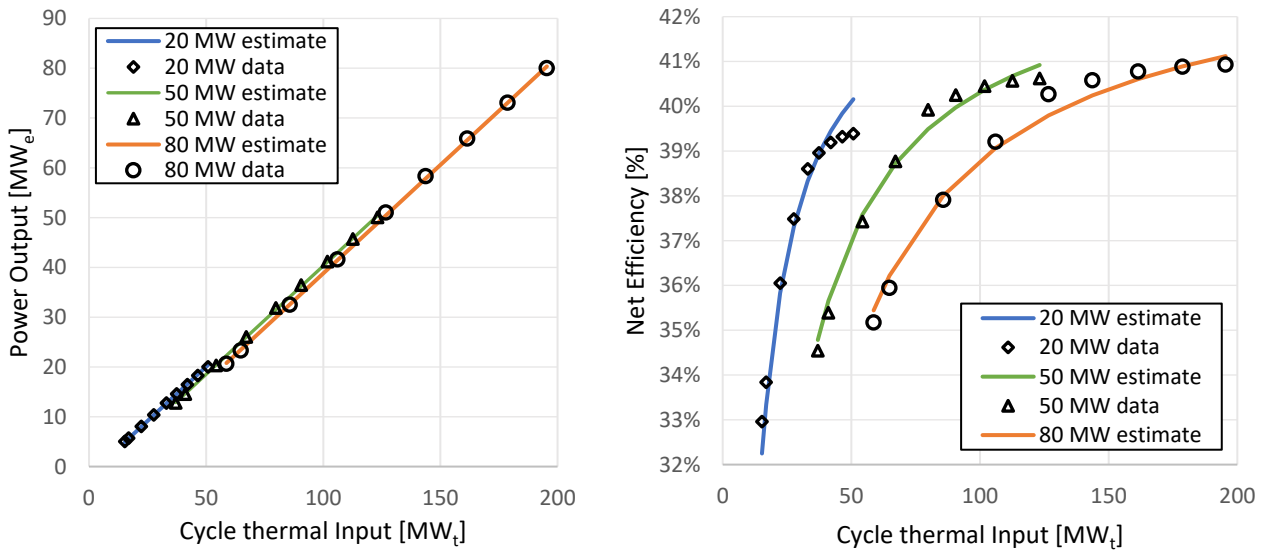

(a) (b)

Figure 9 – Size and part-load effect (a) on the electrical power produced and (b) on the net electrical efficiency of the PB

It is important to notice that the outlet MS temperature of the PB depends on the cycle load. To keep the energy balance of the cold storage tank linear (see next subsection), we need to introduce in the variables of the model the enthalpy flows associated with the MS mass flow rate entering and existing the PB, defined according to Eq. (9), (10) and (11).

$$\dot{Q}_{PB,t}^{in} = \dot{H}_{PB,t}^{in} - \dot{H}_{PB,t}^{out} \qquad \forall t \in T \quad (9)$$

$$\dot{H}_{PB,t}^{in} = \dot{m}_{PB,t}^{in} \cdot h_{PB,t}^{in} \qquad \forall t \in T \quad (10)$$

$$\dot{H}_{PB,t}^{out} = \dot{m}_{PB,t}^{out} \cdot h_{PB,t}^{out} \qquad \forall t \in T \quad (11)$$

The enthalpies and internal energies of MS have been defined taking as reference temperature ($\hat{T}_{ref}$) 245°C, a value sufficiently far from the crystallization limit so that the ideal liquid model can be assumed for MS.

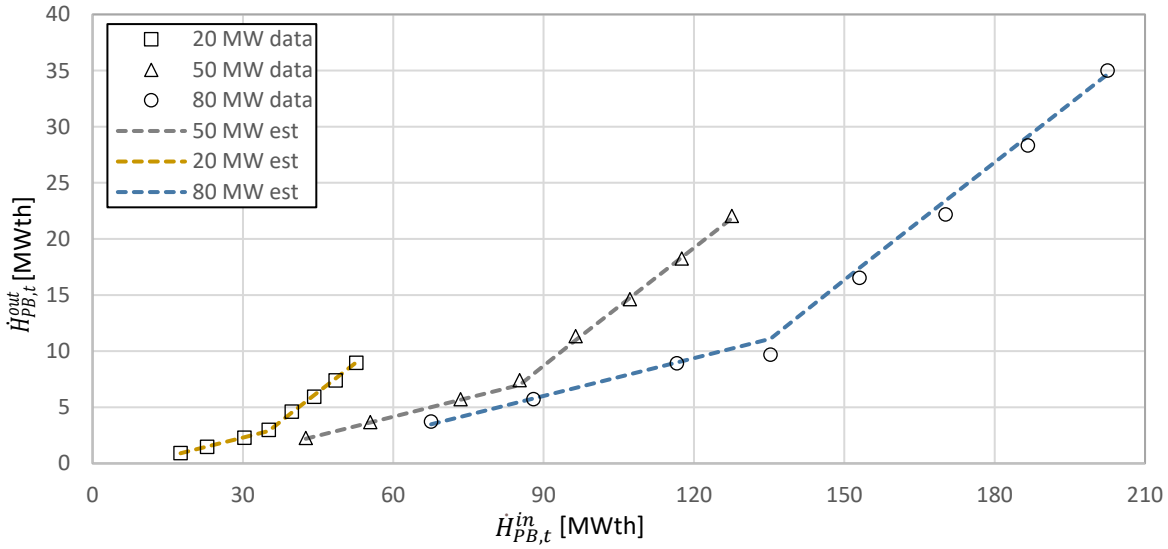

Figure 10 – Best fit of the data related to the salt residual enthalpy for different PB load and size ranges

In particular, we are interested in keep track of the enthalpy content of the MS discharged from the PB ($\dot{H}_{PB,t}^{out}$): as visible in Figure 10, such variable depends in a non-smooth way on the enthalpy flow of MS entering the PB (correlated with PB load). The particular shape of the function and the slope change derive from the variation in part-load control strategy of the steam cycle: as previously explained, sliding pressure regulation is adopted throughout all turbine stages from the 100% down to 60% load, then for lower solar mass flow rates (< 60% load) the pressure of the first regenerator is kept constant by adjusting the turbine re-admission valve so as to keep high the pressure of bleed sent to the feedwater preheater. The non-smooth shape of such nonlinear curve linking $\dot{H}_{PB,t}^{in}$ and $\dot{H}_{PB,t}^{out}$ has been best-fitted with a piecewise linear function defined over two segments, segment A and B, as reported in Eq. (12). The linear function considers the effect of the load with the variable $\dot{H}_{PB,t}^{out}$ (proportional to the flow rate of MS entering the PB through the coefficient $\hat{Y}_{1,j}$) and the dependence on the PB size by means of the coefficient $Y_{2,j}$.

$$\dot{H}_{PB,t}^{out} = \sum_{j=A,B} \left(\hat{Y}_{1,j} \cdot \dot{H}_{PB,t}^{in} + \hat{Y}_{2,j} \cdot \dot{H}_{PB,max}^{in} \right) \qquad \forall t \in T \quad (12)$$

Table 6 – Best fit coefficients of the piecewise linear Eq. (12)

Segment	$\hat{Y}_{1,j}$ $[MW_{th}/MW_{th}]$	$\hat{Y}_{2,j}$ $[MW_{th}/MW_{th}]$
A (< 60% load)	0.1124	-0.0203

B (> 60% load)	0.3484	-0.1773

Figure 10 provides a visual representation of Eq. (12) comparing the estimated values with the data determined with Thermoflex. Note that the residual enthalpy $\dot{H}_{PB,t}^{out}$ assumes always positive values as the temperature of the MS leaving the PB never goes below the value assumed as reference (245°C).

4.4 TES model and linearization

The variable temperature of the MS discharged from the PB, the heat losses from the storage tank and the thermal power used during night for the PB and SF warm-keeping may reduce the temperature of the cold storage tank with the risk of approaching the MS solidification temperature (238°C according to [33]p).

$$\dot{H}_{SF,t}^{in} = \dot{m}_{SF,t}^{in} \cdot h_{SF,t}^{in} \qquad \forall t \in T \qquad (13)$$

$$\dot{H}_{SF,t}^{wk} = \dot{m}_{SF,t}^{wk} \cdot h_{SF,t}^{wk} \qquad \forall t \in T \qquad (14)$$

$$U_t^{cold} = M_t^{cold} \cdot u_t^{cold} \qquad \forall t \in T \qquad (15)$$

Thus, it is necessary to consider the variation of cold storage tank temperature in the plant dispatch by writing its energy and mass balance equations. With reference to Figure 11, $\dot{Q}_{loss,t}^{cold}$ denotes the thermal power lost from the cold storage tank (assumed as a percentage of the contained internal energy U_t^{cold}), $\dot{H}_{SF,t}^{in}$ denotes the product of mass flow rate and enthalpy of the MS sent to the solar field (see Eq. (13)), $\dot{H}_{SF,t}^{wk}$ denotes the return mass flow rate times enthalpy of the MS used for warm keeping during night (see Eq. (14)), $\dot{H}_{PB,t}^{out}$ is the residual enthalpy of the MS flow coming from the power block, while $\dot{Q}_{EH,t}^{cold}$ denotes the heating power provided with the EH (used to prevent MS solidification in long cloudy periods), U_t^{cold} represents the internal energy of the cold tank and is defined in Eq. (15). Specific enthalpies ($\mathrm{h}_{SF,t}^{in}$, $h_{SF,t}^{wk}$) and internal energy (u_t^{cold}) of MS are defined assuming the same reference temperature ($\hat{T}_{ref}$ = 245 °C).

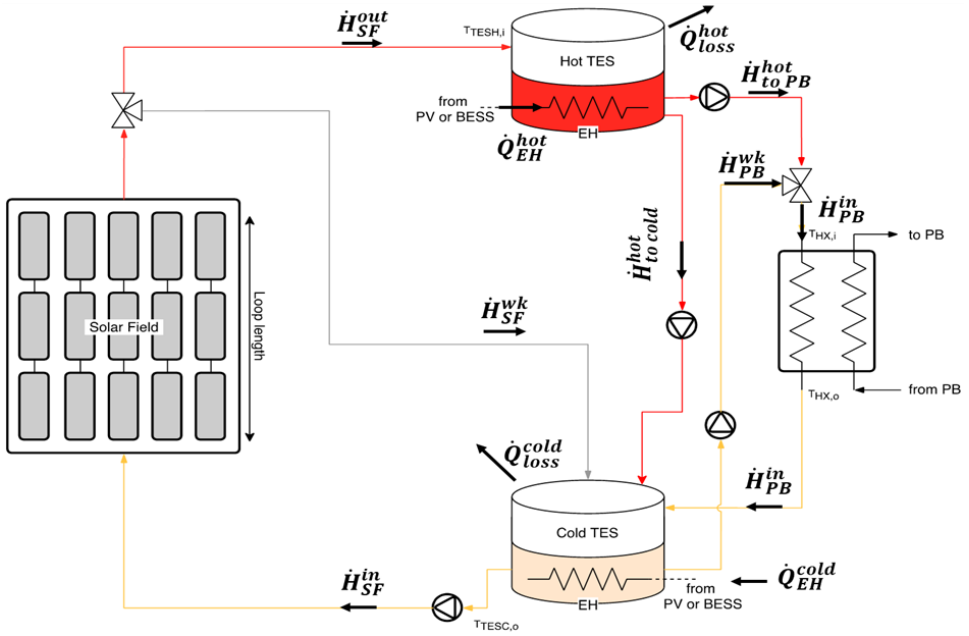

Figure 11-CSP section layout with the SF and TES main operating variables

As far as the hot tank is concerned, it receives a hot flow of MS coming from the SF ($\dot{H}_{SF,t}^{out}$) plus the thermal power from the EH ($\dot{Q}_{EH,t}^{hot}$) and it provides hot MS to the PB ($\dot{H}_{toPB,t}^{hot}$) and, in case of necessity, a hot bypass ($\dot{H}_{tocold,t}^{hot}$) flow directly to the cold tank to rise MS temperature.

The plain formulation of the TES model would involve mass flow rates and temperatures as variables in order to track the evolution of the cold storage temperature. However, such formulation would lead to nonlinear terms (products between mass flow rates and temperatures) as shown in Eq. (16) and (17).

$$U_t^{cold} - U_{t-1}^{cold} = \left(\dot{m}_{PB,t}^{out} \cdot \hat{c}_{MS}^{mean} \cdot T_{PB,t}^{out} + \dot{m}_{tocold,t}^{hot} \cdot \hat{c}_{MS}^{mean} \cdot T_{tocold,t}^{hot} + \dot{m}_{SF,t}^{wk} \cdot \hat{c}_{MS}^{mean} \cdot T_{SF,t}^{wk} + \dot{Q}_{EH,t}^{cold}\right) - \left(\dot{m}_{SF,t}^{in} \cdot \hat{c}_{MS}^{mean} \cdot T_{SF,t}^{in} + \dot{m}_{PB,t}^{wk} \cdot \hat{c}_{MS}^{mean} \cdot T_{PB,t}^{wk} + \dot{Q}_{loss,t}^{cold}\right) \quad \forall t \in T \quad (16)$$

$$M_t^{cold} - M_{t-1}^{cold} = \left(\dot{m}_{PB,t}^{out} + \dot{m}_{tocold,t}^{hot} + \dot{m}_{SF,t}^{wk}\right) - \left(\dot{m}_{SF,t}^{in} + \dot{m}_{PB,t}^{wk}\right) \quad \forall t \in T \quad (17)$$

To write Eq. (16), the mean average value of the specific heat capacity of the MS over the relevant range of temperatures ($\hat{c}_{p,MS}^{mean}$) has been used, considering the correlation in [21] to take into account the dependence on the temperature (Eq. (18)).

$$\hat{c}_{MS}^{mean} = \frac{1}{\left(\hat{T}_{max} - \hat{T}_{min}\right)} \int_{\hat{T}_{min}}^{\hat{T}_{max}} 1.443 + 0.000172 \cdot T \cdot dt \quad (18)$$

To avoid such nonlinear terms which are not suitable for the MILP formulation, we reformulated the cold tank energy balance (16) using the enthalpy and the internal energy of MS, as follows:

$$U_t^{hot} = U_{t-1}^{hot} + \left(\dot{H}_{SF,t}^{out} + \dot{Q}_{EH,t}^{hot}\right) - \left(\dot{H}_{toPB,t}^{hot} + \dot{H}_{tocold,t}^{hot}\right) - \dot{Q}_{loss,t}^{hot} \quad \forall t \in T \quad (19)$$

$$U_t^{cold} = U_{t-1}^{cold} + \left(\dot{H}_{PB,t}^{out} + \dot{H}_{tocold,t}^{hot} + \dot{H}_{SF,t}^{wk} + \dot{Q}_{EH,t}^{cold}\right) - \left(\dot{H}_{SF,t}^{in} + \dot{H}_{PB,t}^{wk}\right) - \dot{Q}_{loss,t}^{cold} \quad \forall t \in T \quad (20)$$

The heat losses in the two storages tanks ($\dot{Q}_{loss,t}^{hot}$, $\dot{Q}_{loss,t}^{cold}$) have been estimated with two separated equations, Eq. (21) and (25). The equations express, instant by instant, the thermal losses of the tank as a function of the energy content, thought the first coefficient $\widehat{w}_1$, and the maximum level (which is related to the tank size) via the coefficient $\widehat{w}_2$, plus a constant term ($\widehat{w}_3$) that represent the losses when the tank is empty or at its minimum level. The linear expression have been derived starting from the values reported in [38] for the two tanks with temperature levels 565°C/290°C. In particular, the correlation in [38] is exploited to derive the heat losses for different tank sizes with the same H/D ratio. The data obtained in this way have been subsequently fit with a multi-linear regression by tuning the coefficients $\widehat{w}_1$, $\widehat{w}_2$ and $\widehat{w}_3$ for each tank, reported in Table 7. The mean error between the heat loss data and the ones computed with the correlation in Eq. (21) and (25) is respectively 1.2% and 1% for the heat and the cold tank.

$$\dot{Q}_{loss,t}^{hot} = \widehat{w}_1^{hot} \cdot U_t^{hot} + \widehat{w}_2^{hot} \cdot E_{max}^{hot} + \widehat{w}_3^{hot} \qquad \forall t \in T \qquad (21)$$

$$\dot{Q}_{loss,t}^{cold} = \widehat{w}_1^{cold} \cdot U_t^{cold} + \widehat{w}_2^{cold} \cdot E_{max}^{cold} + \widehat{w}_3^{cold} \qquad \forall t \in T \qquad (22)$$

Table 7 - Linearization coefficients for the hot and cold tank, respectively

Coefficient	$\widehat{w}_1\ [kW_{th}/kWh_{th}]$	$\widehat{w}_2\ [kW_{th}/kWh_{th}]$	$\widehat{w}_3\ [kW_{th}]$
Hot tank	0.035	0.088	58.199
Cold tank	0.103	0.276	23.334

In order to link the cold tank internal energy U_t^{cold} with the MS temperature and mass of contained MS (M_t^{cold}), we approximated the product of the two variables with the "McCormick envelopes" [39], Eq. (23)-(24). By writing the internal energy of the cold tank as in Eq. (23) and (24) it is possible to ensure that the temperature of the MS is always higher than the minimum ($\hat{T}_{min}$) and lower than the maximum ($\hat{T}_{max}$) value for each operating condition of the SF. Considering a large safety margin from the molten salts freezing temperature (238°C), $\hat{T}_{min}$=275°C and $\hat{T}_{max}$=300°C have been assumed.

$$U_t^{cold} \leq U_{max,t}^{cold} = M_t^{cold} \cdot \hat{c}_{v,MS}^{mean} \cdot \left(\hat{T}_{max} - \hat{T}_{ref}\right) \qquad \forall t \in T \qquad (23)$$

$$U_t^{cold} \geq U_{min,t}^{cold} = M_t^{cold} \cdot \hat{c}_{v,MS}^{mean} \cdot \left(\hat{T}_{min} - \hat{T}_{ref}\right) \qquad \forall t \in T \qquad (24)$$

Although the proposed methodology for the linearization of the product between mass and temperature does not allow optimizing and tracking, instant by instant, the exact temperature profile of the salts, such an approach guarantees that the MS temperature in the cold TES side is always within the desired range (275-300°C).

4.5 Economic models of subunits

Table 8 summarizes all the economic assumptions for each plant component.

Table 8 - Plant techno-economic assumptions

Component	Parameters	Value	Units	Reference
Plant (overall)	Useful life	25	years	assumed
	Interest rate	8%	-	assumed
	Land purchase cost	3	€/m^2	[40]
	Contingencies cost	7%	% investment	[41]*
	EPC costs	11%	% investment	[41]*
PV (multi-crystalline silicon)	Investment cost	713.8	€/kW	[3]*
	O&M fix costs	15.5	€/kW/y	[3]*
BESS (lithium-ion)	Energy-related inv. cost	257	€/kWh	[2]*
	Power-related inv. cost	224	€/kW	[2]*
	O&M fix cost	12	€/kW/y	[2]*
SF (linear Fresnel)	Investment cost**	169.4	€/m^2	[41]*
	Land preparation cost	17.2	€/m^2	[41]*
TES (two-tanks direct)	Investment cost	27.5	€/kWh	[41]*
	O&M fix cost	0.3	€/kWh	[41]*
EH (electric heater)	Investment cost	80	€/kW	[40]
Power block (Rankine cycle)	Investment cost***	1000-1780	€/kW	Thermoflex [27] + SAM [26]*
	O&M fix cost	10.8	€/kW/y	[41]*
	O&M variable cost	3.4	€/MWh	[41]*
	Hot start-up cost	31	€/MW/start	assumed
	Warm start-up cost	50	€/MW/ start	assumed
	Cold start-up cost	65	€/MW/ start	assumed
* assuming a euro/dollar exchange rate of 0.86				
** includes SF mirror cost, HTF system cost, pump and heat exchangers costs.				
*** variable with PB size. Balance of plants included.				

The value assumed for the land cost refers to the purchase of a plot of land in the south of Italy which cannot be directly employed for farming applications. The cost related to the installation of PV panels has been derived from Irena [3] as well as the fixed O&M costs of this component. The investment cost of the BESS is split into two contributions: one related to battery capacity and one related to its power rating. These values have been taken from the NREL study in [2] together with the assumed fixed O&M cost of the battery, computed as 2.5% of the capital cost. The SAM cost database [41] is considered as reference for the cost models of the CSP section (SF, TES and PB subsystems) and the same contingencies and EPC costs have been assumed.

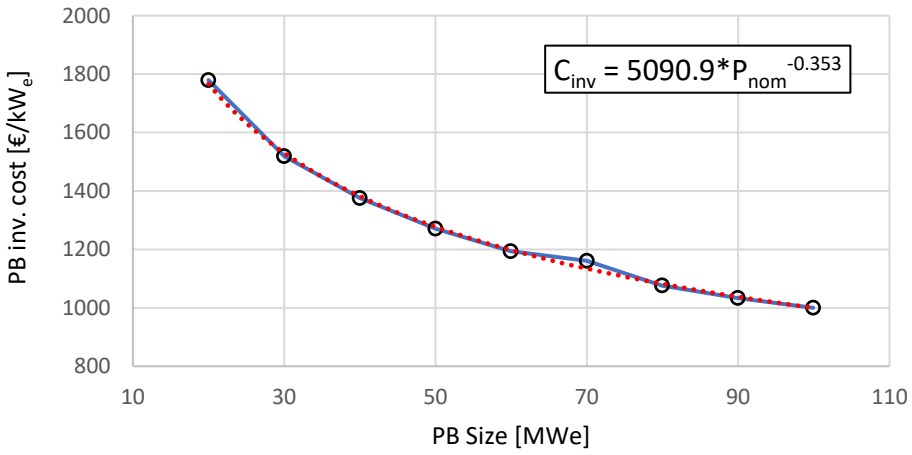

Figure 12 - PB specific investment cost data points, best fit non-linear function (in red) and piecewise linear approximation (in blue)

The only exception is the correlation used to estimate the PB specific investment cost as a function of its nominal size which has been taken from the Thermoflex database. As the size effect can be neglected for most of the modeled components since they are modular, this is not the case for the PB whose investment costs benefit of the economic of scale. For this reason, several cost data points have been estimated via the PEACE (Plant Engineering and Construction Estimator) module of Thermoflex and then they have been interpolated via a non-linear power function that expresses the specific investment cost a function PB nominal power. Considering the significant cost discrepancy obtained for a 50 MW power block with respect to the SAM cost database, it has been chosen to re-scale the obtained cost power function considering the SAM specific costs. Because of the non-linear trend, this function cannot be directly employed within the MILP model: therefore a piecewise linear approximation of the data points has been incorporated into the MILP formulation to estimate the PB capital cost taking into account the size effect. Figure 12 shows the points related to the investment cost data of the PB section computed with Thermoflex, the resulting non-linear trendline and the piecewise linear interpolation. Finally, three different start-up types with their own start-up costs have been included in the PB operation: hot, warm and cold. The selection of the start-up mode is done according to the number of hours the steam cycle has been off: < 16 hours for the hot start-up, between 16 and 64 for the warm one and > 64 for the cold start [34].

5 Simultaneous design-operation optimization

5.1 Problem statement

The design optimization problem of the hybrid plant (operating as a VPP) can be stated as follows. Given:

- the expected hourly generation profiles of non-dispatchable sources (PV electricity and SF thermal production), specific per unit of area
- the electricity demand profile
- all the technical and economical correlations of each plant component (PV, PB, TES, SF, etc) as a function of size and part-load/sun radiation

it is desired to determine the optimal values of (i) the size (area/land used) of PV panels and SF, (ii) the sizes of the different system components (TES, PB and BESS) while taking into account the optimal operation of the plant (on/off and loads) across an average year.

The objective function is the minimization of the TAC, which includes the costs related to unit sizing (investment) and operation (O&M costs).

The problem constraints to take into account are:

- total land area availability for PV and SF collectors
- minimum and maximum component sizes
- minimum and maximum temperature of molten salts inside the cold tank
- BESS maximum charge and discharge rates
- PB operating map (min/max load, part-load efficiency map)
- start-up ramping trajectory of the PB
- energy and mass balances
- minimum dispatchability level required to the system, defined as the percentage of the imposed load that the hybrid plant is able to cover along the year

5.2 Definition of typical operating periods

Given the complexity of the optimization problem and the large number of variables and constraints involved, a solution with an hourly resolution that considers an entire year as an optimization horizon would require an excessive computational effort, since the solution time increases exponentially with the number of time steps considered inside the optimization horizon. For this reason, in order to tackle large-scale problems capable of simultaneously optimizing the design and management of the plant, it is common practice to reduce the temporal dimension of the problem via clustering techniques [42], which allows to identify the most "representative" periods of the year. These periods, whose length can vary from a single day to an entire week, are compared based on their characteristics (e.g. solar, PV production, electricity demand, etc.) and then aggregated each other by the clustering algorithm according to a similarity criterion. By doing so, is possible to reconstruct the input profiles over the entire year with the periods selected by the clustering procedure, also called "design " or "typical" periods (TP), thus reducing the time scale of the optimization problem.

Among various clustering algorithms available in literature [42], k-MILP [43] has been selected for its ability to identify, other than the most representative periods of the year, also the extreme ones, essential for an accurate plant design and sizing. The extremes are those periods of the year where the maximum or the minimum value of a certain profile (e.g. renewable production, load) occurs. Therefore, such periods result particularly critical for the design of plant components and must be included in the optimization horizon.

It is important to point out that the MILP model formulated on TP assumes a periodic constraint on the state of charge of the storage (the storage level at the end of the TP must be equal to the level at the beginning) and status (on/off and load) of the units (same status at the beginning and end of the TP). This constraint is necessary otherwise in the reconstruction of the syntetic year with TPs, there would be a discontinuity between the end of a TP and the beginning of the subsequent one.

Thus, the duration of the TP must be a multiple of the periodicity of the phenomena occurring in the system: in this way, these phenomena are present also in the TP with complete cycles and the cyclic constraint on the storage and units status is coherent with the periodicity of these phenomena.

The periodic phenomena involved in the plants considered in this work are:

- the periodicity of the electricity demand profiles and solar radiation profiles. These profiles have a general periodicity of 24 hours. However, in the considered site, there may be long periods without sun radiation due to the presence of clouds for three days. Looking at the historical radiation profiles, these cloudy periods can occur in winter and summer with similar

durations. Thus, to catch this cyclic trend, it is necessary to consider a TP length equal to at least three days

- the time horizon considered by the management strategy of the storage tank. This time horizon depends on the availability of accurate solar radiation forecast and the capacity of the storage system (the larger, the longer the time horizon). Assuming that the maximum installable storage capacity can cover 24 h of operation and the radiation forecast accuracy is good for a horizon of 2-3 days maximum, it is possible to state that a TP duration of 3 days (72 hours) does not over-constrain the thermal storage management.

In light of the last point, we have selected a TP duration of 3 days (72 hours) and used the k-MILP [43] clustering approach to find extreme (EP) and typical (TP) periods.

As for the number of TPs and EPs, we have considered 3 EPs and 6 EPs. As for the EPs, the three extreme periods identified by clustering algorithm correspond to the periods with the (i) maximum SF generation, the (ii) minimum of PV production and the (iii) maximum electricity demand. As for the TPs, we assessed the accuracy by comparing the actual duration curves of solar production (of the reference year) with those obtained with the TPs, as reported in Figure 13. The duration curves of Figure 13 have been obtained by sorting in descending order the hourly values of the specific production profile of the PV and SF respectively. The blue line is obtained with the actual profiles extracted from SAM while the orange line with the 6 TPs and 3 EPs selected by the k-MILP algorithm. The profile of specific SF production stops at 3000 h approximately because there are only about 3000 hours per year with sufficient direct radiation (sunny hours, not too cloudy neither dark).

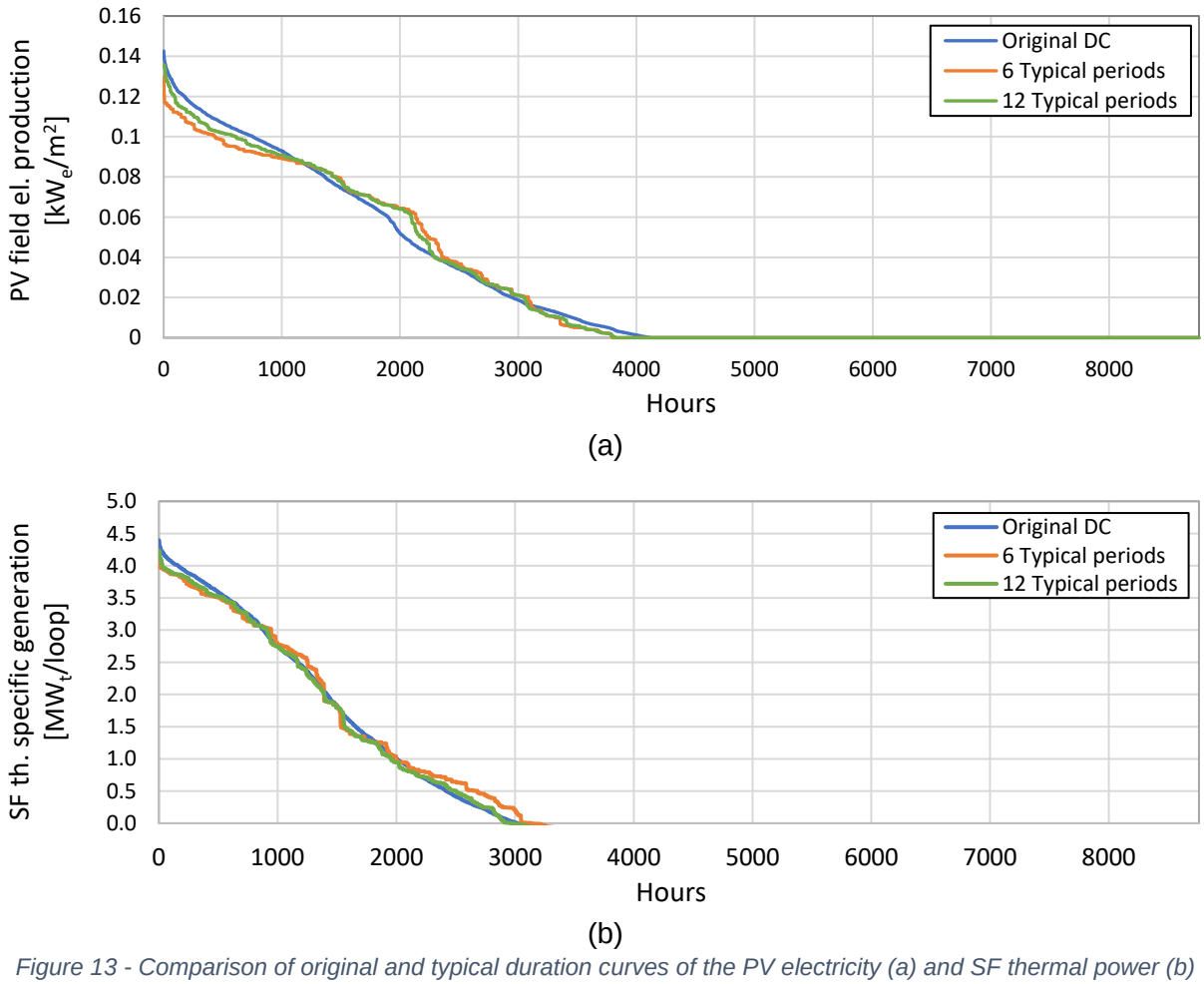

Figure 13 - Comparison of original and typical duration curves of the PV electricity (a) and SF thermal power (b) production, using 6 and 12 typical periods.

Figure 13b shows that the orange line (duration curve approximated with 6 TPs and 3 EPs) approximates quite well the specific thermal production of the SF. On the other hand, Figure 13a indicates that the orange line overestimates the PV production in the medium-low range (0.04-0.06 kW/m^2) and underestimates in the high range (0.09-0.12 kW/m^2). Such approximation improves slightly when increasing the number of TPs to 12 [44]. For this reason, we have performed preliminary computational tests aimed at solving the MILP optimization problem with 12 TPs but the required computational time (>1 hour per run) turned out to be excessive to run all the different cases considered in this analysis . As a comparison, solving the MILP with 6 TPs takes approx. 10 minutes per case. Moreover, for the first tested cases, we have noticed that the optimal design of the hybrid plant obtained considering 12 TPs is very close to that obtained with 6 TPs (i.e., same layout and differences in unit sizes and objective function < 2%).

The profiles of the 6 TPs are reported in Figure 14 while the number of occurrences in the year is detailed in Table 9 (the number of occurrences of a TP is number of periods of the reference year classified by the clustering algorithm as similar to each TP).

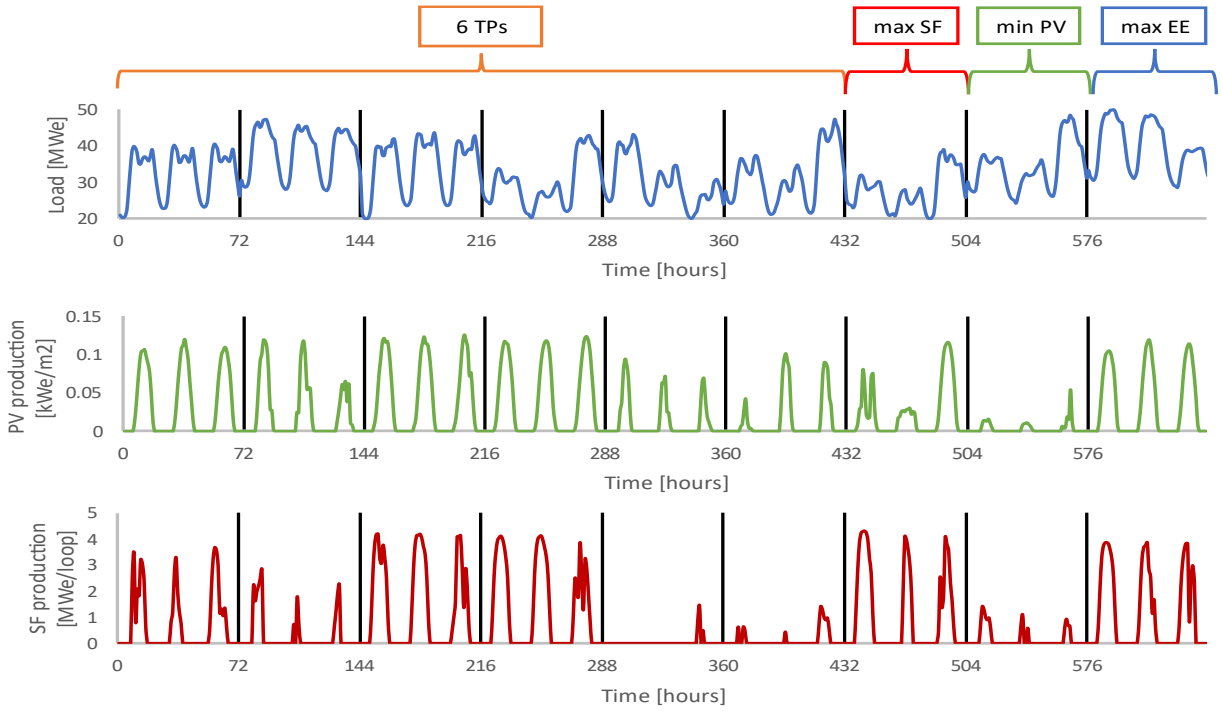

Figure 14 – Selected typical and extreme periods

Table 9 - Typical periods occurrences over the year. The last three TPs weight one since they are EPs

TP	TP #1	TP #2	TP #3	TP #4	TP #5	TP #6	EP #1	EP #2	EP #3
Weight	25	9	20	23	18	24	1	1	1

5.3 MILP model

The simultaneous design and operation optimization of energy systems is a complex task that requires handling a problem with the design variables, and several tens of operating constraints (performance maps, ramping constraints, energy balance, etc) and tens of operating variables (on/off and loads of generators, state of charge of storages, etc) for each time step. Even if the operation is considered for a limited set of representative operating periods, the optimization problem turns out to have thousands of variables and constraints. Moreover, the problem is mixed integer (since it involves binary variables to model the on/off status of the units) and nonlinear (due to the

performance maps and cost correlations of the units). Such class of problems, called MINLP (mixed integer nonlinear programs), is extremely difficult to solve, especially for large scale problems (see, e.g., the tests reported in [45] and [46] for similar types of problems). As shown in [45], [46] and [37], it is preferable to linearize the problem and obtain a MILP which can be solved to global optimality with efficient branch and bound solvers such Gurobi [47] and Cplex [48]. This represents today the most common methodology applied in the design and operation optimization of MES [37] and microgrids [49][50]. Hence, the problem described in Section 5.1 has been formulated as a MILP in order to exploit the convergence speed and convergence guarantees of the available MILP solvers.

The MILP model includes the following groups of variables:

- design variables such installed area of renewables (A^{PV}, A^{SF}), PB nominal thermal power ($\dot{H}^{in}_{PB,max}$), storage capacities (E_{BESS}, E_{TES}), EHs rated power (P_{EH})
- variables related to the operating (mass and enthalpy flows, production levels, power exchanges) and commitment (PB on/off, start-up and shut-down) status of dispatchable components

The constraints of the MILP model are the linearized version of the equations already shown describing the performance and costs of the plant sub-units (PV, SF, TES, etc.). In particular, Eq. (1) and (4) link the installed area with the specific production profile of renewable sources (PV, SF) determining the available generation in each hour of the optimization horizon, Eq. (5) computes the SF pumps consumptions, Eq. (6) expresses the input-output relationship related to the PB operation, considering the size and load effect on performances, while Eq. (11)-(29) control the TES management and all the associated energy flows between TES, SF and PB sections.

$$z^{PB}_t - z^{PB}_{t-1} = \delta^{PB}_{on,t} - \delta^{PB}_{off,t} \qquad \forall t \in T \qquad (25)$$

$$\delta^{PB}_{on,t} + \delta^{PB}_{off,t} \leq 1 \qquad \forall t \in T \qquad (26)$$

$$P^{PB}_{out,t} - P^{PB}_{out,t-1} \leq \hat{R}^{lim}_{up} \qquad \forall t \in T \qquad (27)$$

$$P^{PB}_{out,t-1} - P^{PB}_{out,t} \leq \hat{R}^{lim}_{down} \qquad \forall t \in T \qquad (28)$$

In addition, Eq. (25)-(26) defines the PB commitment status and Eq. (27)-(28) is necessary to impose the ramping limits in the upward and downward directions during PB operation. Eq. (29) ensures that the actual TES level is always lower or equal to its capacity. Eq. (30) is an analogous equation linking the battery storage state of charge (SOC^{BESS}_t) with its maximum capacity(E_{BESS}). The dynamic SoC evolution of the BESS in two consecutive timesteps is described by Eq. (31) and Eq. (32)-(33) limits the maximum charge and discharge power from the BESS according to its c-rate ($\hat{C}^{BESS}_{rate}$). Regarding the battery degradation, we neglected the loss of capacity and max discharge rate due to aging, but, we consider the BESS life degradation via an equivalent O&M accounting for its replacement [51]. In particular we used the “throughput model”: the O&M replacement cost can be computed dividing the investment cost of the battery by the total energy throughput over its lifetime, estimated assuming the number of equivalent full cycles (i.e. considering 100% dept of discharge) the BESS can sustain before being replaced [52].

$$U^{hot}_t \leq E_{TES} \qquad \forall t \in T \qquad (29)$$

$$SOC_t^{BESS} \leq E_{BESS} \qquad \forall t \in T \quad (30)$$

$$SOC_t^{BESS} = SOC_{t-1}^{BESS} + \left(P_{ch,t}^{BESS} \cdot \hat{\eta}_{ch}^{BESS} - P_{disch,t}^{BESS} / \hat{\eta}_{disch}^{BESS}\right) \qquad \forall t \in T \quad (31)$$

$$P_{ch,t}^{BESS} \leq \hat{C}_{rate}^{BESS} \cdot E_{BESS} \qquad \forall t \in T \quad (32)$$

$$P_{disch,t}^{BESS} \leq \hat{C}_{rate}^{BESS} \cdot E_{BESS} \qquad \forall t \in T \quad (33)$$

Eq. (34) defines the EHs rated power as the maximum power exchanged through the EH in each timestep and Eq. (35)limits the total land available for renewable installation.

$$\frac{\dot{Q}_{EH,t}^{hot}}{\hat{\eta}_{EH}} \leq P_{EH} \qquad \forall t \in T \quad (34)$$

$$A^{PV} + A^{SF} \leq \hat{A}_{tot} \qquad \forall t \in T \quad (35)$$

Eq. (36) reports the electricity energy balance of the plant: the electricity discharge from the battery ($P_{disch,t}^{BESS}$) or produced by the PV field ($P_{out,t}^{PV}$) and the PB of the CSP section ($P_{out,t}^{PB}$) can be either used to charge the battery ($P_{ch,t}^{BESS}$), power the EHs ($\dot{Q}_{EH,t}^{hot}$, $\dot{Q}_{EH,t}^{cold}$) or exported to the grid (P_t^{grid}). Finally, Eq. (37)is used to impose the desired plant dispatch level (e.g. 40%, 60%, etc.), expressed as a percentage (p_d) of the integral value of the yearly electricity demand imposed.

$$P_{out,t}^{PV} + P_{out,t}^{PB} + \left(P_{disch,t}^{BESS} - P_{ch,t}^{BESS}\right) - \frac{\dot{Q}_{EH,t}^{hot}}{\hat{\eta}_{EH}} - \frac{\dot{Q}_{EH,t}^{cold}}{\hat{\eta}_{EH}} = P_t^{grid} \qquad \forall t \in T \quad (36)$$

$$\sum_{t \in T} P_t^{grid} \geq \hat{p}_d \cdot \sum_{t \in T} \hat{D}_t \qquad \forall t \in T \quad (37)$$

The objective function of the model is the minimization of the TAC, defined in Eq. (38) as the sum of all the capital and operational expenditures. The capital expenditures include all the costs related to the purchase and installation of plant components and they are annualized by means of the Capital Recovery Factor (CRF) that, according to Eq. (39) [53], can be estimated starting from the plant lifetime ($lifetime$) and interest rate (r). Another economical indicator for the plant performances evaluation is represented by the LCOE, which is a measure of the cost of the energy produced from the plant. The LCOE is the ratio between the TAC and the total energy produced over the year ($\mathrm{E_{prod.}}$), expressed as the sum of the total energy exported to the grid. It must be noted that, once the fraction of load to satisfied is chosen ($\hat{p}_d$), as optimization problem parameter, a lower bound on the total energy that will be generated by the plant is enforced by constraint (37). Therefore, since the annual energy produced is fixed, in this case the minimization of the TAC corresponds to the minimization of the LCOE itself (the denominator of Eq. (40) is constant).

$$TAC = CAPEX \cdot CRF + OPEX \quad (38)$$

$$\mathrm{CRF} = \frac{\mathrm{r}}{1 - (1 - \mathrm{r})^{-\mathrm{lifetime}}} \quad (39)$$

$$\mathrm{LCOE} = \frac{\mathrm{TAC}}{\mathrm{E_{prod.}}} = \frac{\mathrm{TAC}}{\sum_{t \in T} P_t^{grid}} \quad (40)$$

Table 10 reports the lower and upper bounds of the design optimization variables considered in the optimization problem.

Table 10 - Range of the values of the design optimization variables considered

Optimization variable	Units	Lower bound	Upper bound
PB nominal net power	[MW_e]	10	100
CSP Solar Multiple	[-]	0	5
TES capacity	[hours]	0	24
Number of SF loops	[-]	0	160
SF active surface	[hectares]	0	150
PV installed capacity	[MW_e]	0	260
PV active surface	[hectares]	0	150
BESS capacity	[MWh]	0	500
EH size	[MW_e]	0	100

Considering 6 typical and 3 extreme periods of 72 hours, the MILP features 52935 var and 43547 constraints. It has been solved with Gurobi [47] on a personal computer with an Intel Core i7-10510U CPU and 16GB RAM. The required average computational time to solve one case at 0.5% of the optimality gap is less than 10 minutes. It can be considered a very effective design tool given the high level of detail of the system models, including operational constraints.

6 Results and discussion

In order to assess the benefits of the integration, a comparison between the performances of the hybrid plant and the respective non-hybrid solutions (i.e. stand-alone CSP and PV-BESS) operated separately has been made. A sensitivity analysis on the dispatchability level has been performed and the performances of the various plant configurations have been compared. A focus on the hybrid plant design allowed us to understand how the optimal size of plant components changes according to the desired dispatchability level imposed. The result of the analysis shows that the hybrid solution is able to achieve a lower generation cost while covering a larger fraction of the variable load with respect to non-hybrid solutions. By means of physical integration, even when highly flexible and dispatchable designs are targeted, it is possible to contain the investment cost of the plant and its generation prices.

6.1 Hybrid vs stand-alone plants

Table 11 shows the comparison between the optimal values of the design variables and the main performances of the hybrid plant with respect to the corresponding stand-alone CSP and PV-BESS configurations, respectively. Two levels of integration have been considered for the hybrid system: the physical (with the presence of the EH) and the virtual (without EH) aggregation. The results in Table 11 have been obtained by targeting a minimum dispatchability level equal to 60% of the annual load for all configurations.

Compared to the hybrid system, the CSP configuration is equipped with a larger PB whose nominal power (39.3 MW) is close to the peak of electricity demand (50 MW), since all the electricity generated to cover the variable load should be produced with this component. Because of the presence of the PV, which can boost the daily generation of the plant, the hybrid configuration is characterized by a lower PB size (21.5 MW), close to the mean value of the electricity demand. For the same reason, the number of SF loops required is lower, as well as the SF surface and consequently, the solar multiple is halved with respect to the CSP plant. The TES storage capacity is similar in the two cases, with an optimal value of around 13.5 hours of thermal storage. The PV-BESS configuration to reach the target on the minimum demand relays on the installation of 160.3 MW of PV field equipped with a large battery storage (236.7 MWh). In the hybrid plant, instead, the BESS is never installed since the mechanism of converting the excess PV production into thermal power via the EH is preferred to the use of the battery (the system TES+EH is cheaper).

Regarding the economic performances, for the same share of met demand (60%), the hybrid plant achieves a lower LCOE (138.5 €/MWh) of the respective separated configurations, with a reduction of -35.3% and -47.7% with respect the CSP and PV-BESS, respectively. Both the curtailed fraction of SF and PV production can be reduced by adopting a hybrid layout and the high share of curtailed PV generation can be exploited by the EH to generate additional thermal energy: almost 25% of the total PV production is used to power the EH. In terms of total land requirements, the hybrid case locates in the middle between the PV-BESS (234 hectares) and the more compact CSP layout (177 hectares).

Table 11 - Optimal plant design and main performances for different plant configurations able to follow at least 60% of the targeted annual load

Plant configuration	**PV-BESS**	**CSP**	**Hybrid**	**Hybrid no EH**
PB nominal net power [MW_e]	-	39.34	21.51	26.06
CSP Solar Multiple [-]	-	3.98	1.96	2.65
TES capacity [hours]	-	13.48	13.72	13.67
Number of SF loops [-]	-	93	25	41
SF active surface [m^2]	-	862721	231914	380340
PV installed capacity [MW_e]	160.26	-	108.19	73.53
PV active surface [m^2]	935530	-	631555	429243
BESS capacity [MWh]	236.69	-	0.00	0.00
EH size [MW_e]	-	0.00	35.28	0.00
Fraction of satisfied demand [-]	**60%**	**60%**	**60%**	**60%**
LCOE [€/MWh]	**204.5**	**187.4**	**138.5**	**143.5**
Energy produced [GWh/y]	176.65	168.54	169.31	169.31
Total annual cost [M€/y]	36.13	31.58	23.44	24.29
Plant specific investment cost [€/kW_e]	2012.0	7773.5	1700.8	2320.5
Fraction of PV production to the EH [%]	-	-	25.39	0.0
Fraction of PV production curtailed [%]	20.99	-	3.05	13.96
Fraction of SF production curtailed [%]	-	14.42	8.47	9.06
Number of hours in which the PB is on [hours]	0.00	5708.3	3308.5	3522.8
Total land occupied [hectares]	233.9	176.8	205.4	185.3

In order to assess the benefit of physical PV-CSP integration, the optimization has been repeated with and without the possibility of exchanging energy via the EH. The results demonstrates that the highly integrated solution performs generally better, achieving a 3.6% reduction of LCOE, since the presence of the EH is able to reduce the share of PV curtailed. The two cases present a similar

design: the components of the virtually aggregated system without EH are slightly larger in size (mainly PB and SF). As the only exception, the installed capacity of PV field is reduced because over-production can not by directly exploited to generate heat by means of EH. The share between SF and PV surface is similar with 27% (with EH) and 53% (without EH) of available land allocated to the SF while the remaining 73% (with EH) and 47% (without EH) is for the PV installation.

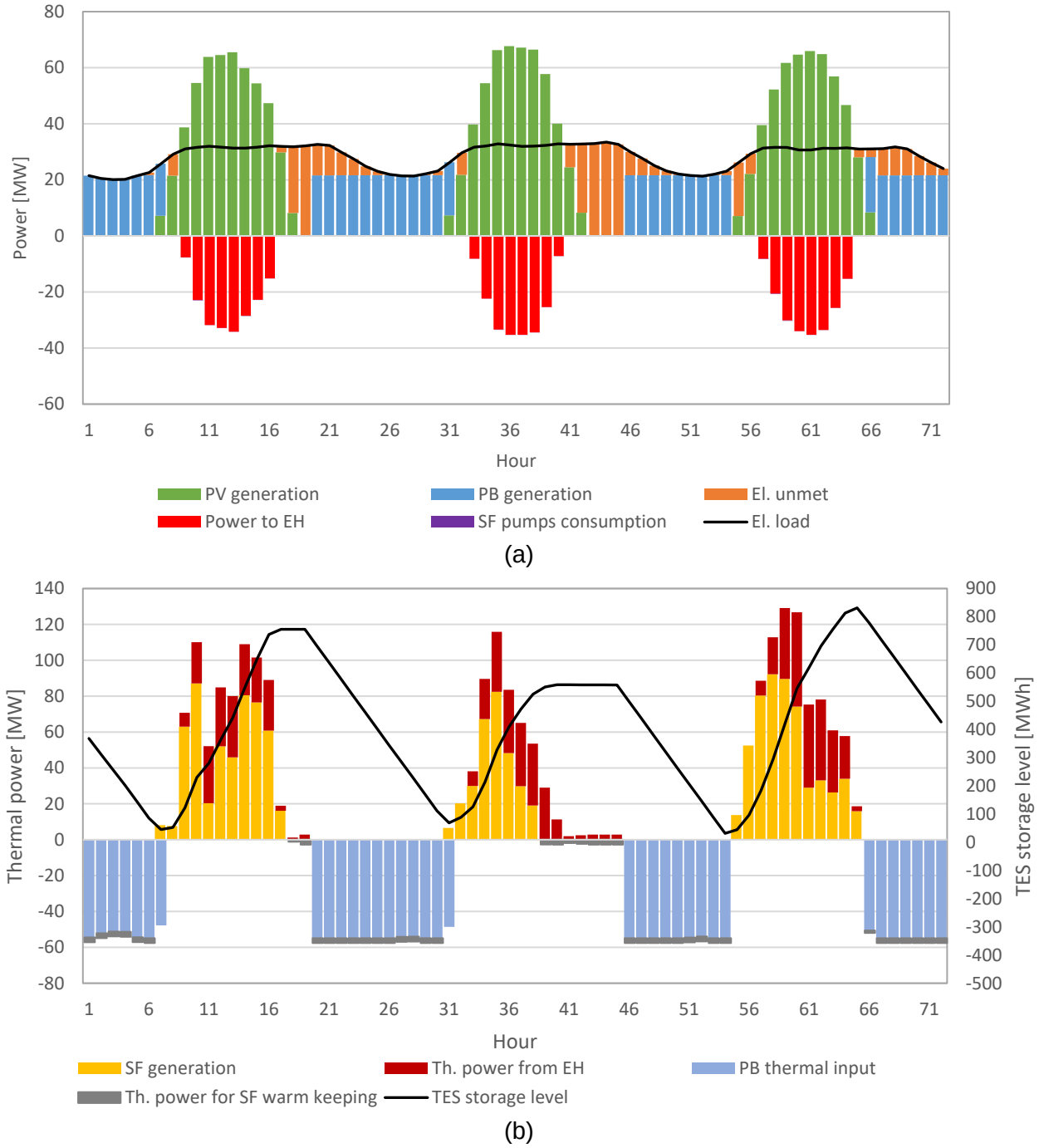

Figure 15 - Sunny day typical operation of the hybrid plant in TP #1. Electricity (a) and heat (b) flows.

Figure 15 shows the operation of the hybrid plant following a variable load for TP #1 occurring 25 times a year (20% of the time) and characterized by a good level of solar radiation. During the hours of the day when the peak of solar radiation occurs, the electricity demand is completely satisfied by the PV production curve (green bars) and the excess electricity is used to power the EH (red bars), increasing the TES energy content. As the PV generation is reduced, the PB is turned on (blue bars) to cover the remaining fraction of demand until its full capacity is fully exploited at night. In the early

hours of the morning, the TES capacity reaches its minimum level and the PB is progressively shut down. These hours of the day, together with the ones in the late afternoon, are the most critical since the PV production cannot deliver its full capacity and therefore the plant is not able to fully meet the demand (orange bars represent the electricity production which is missing to cover the remaining share of the load). Figure 15b reports the thermal management of the TES corresponding to the above-described operation: the heat collected by the solar field (yellow bars) during the day is then used to supply the PB heat exchanger (light blue bars) during the night and partly is employed for warm-keeping purposes (grey bars). It is also visible the contribution of the EH in the increase of the TES level during the central part of the day.

It is important to point out that the choice of the optimizer to install a power block with a size (~ 21 MW) lower than the electricity peak results in a small fraction of unsatisfied electricity demand. By doing so the PB at night can always be operated at full load, maximizing the operating efficiency. A large power block, instead, would have been operated at full load for only few hours when the peak of electric demand occurs while the rest of the day it would be forced to run at part-load, with a lower conversion efficiency. It must be noted that the electricity peak takes place in the central hours of the day, in correspondence to the peak production of PV field. This synergy allows to boost the total electricity production of the plant and, at the same time, allows to contain the PB size.

In the Appendix have been reported the plots related to the operation and the management of the plant in the other typical and extreme periods.

6.2 Sensitivity analysis on the plant dispatchability level

The comparison abovementioned has been repeated for different levels of plant dispatchability (40%-80%) to investigate how the ability to follow an imposed load influences the plant design and performance in terms of LCOE. The result of this analysis is the plot in Figure 16, showing the trend of LCOE of the various plant configurations for different percentages of the annual satisfied demand. While the PV-BESS solution is the best option, in terms of LCOE, to cover up to 50% of annual load, the CSP configuration becomes more convenient in the range 50%-60% than a PV plus battery system. However, if at the beginning the LCOE increase is almost flat, after 60% it starts rising very fast because such dispatchability levels would be hardly achieved by a fully-renewable CSP configuration. At some point, the optimizer is even able to find a feasible solution since no fossil back-up system is present in the CSP layout and it is impossible to operate the plant to meet the demand on days where the solar radiation is particularly low (moreover, issues related to salts freezing may preclude the existence of a solution, especially in absence of the EH).

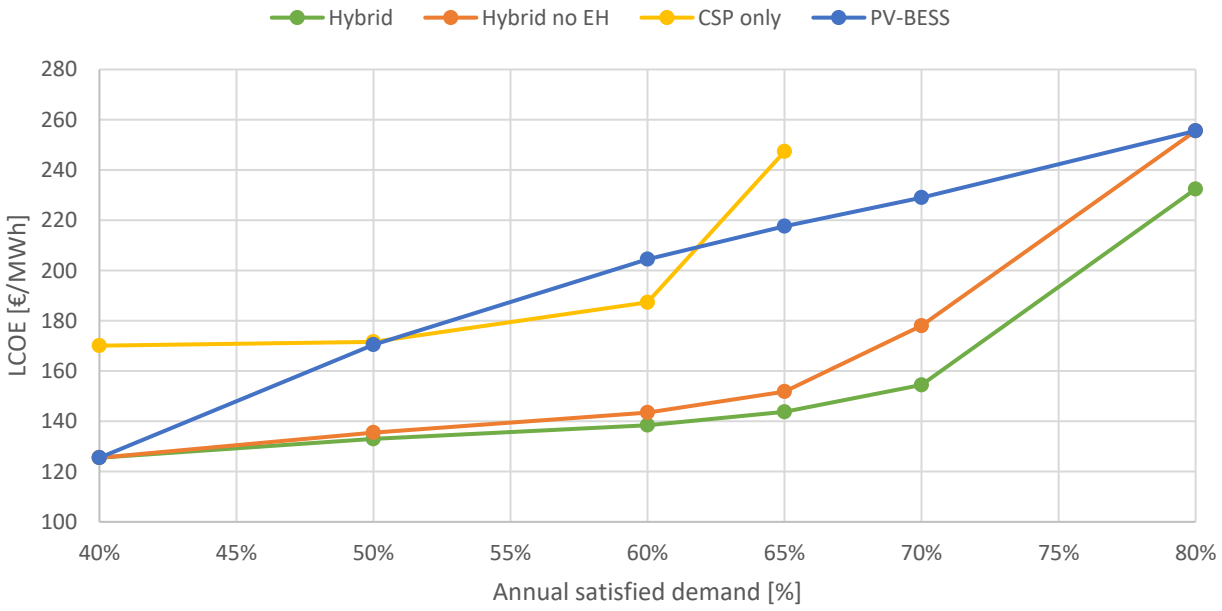

Figure 16 - LCOE of explored plant configurations for different dispatchability levels

Table 12 shows f the optimal size of the plant components for each of the analyzed configurations and for each investigated level of dispatchability. Going from 40% to 80% percentage of dispatchability, the PV-BESS configuration needs to double the size of the PV and install a 10 times larger BESS capacity. In particular, the PV and BESS sizes increase approx. linearly up to 70% dispatchability with an average rate of 2.5 MW and 10 MWh per percentage of dispatchability (respectively). Above 70% dispatchability, the increase rate of the PV capacity becomes more than double (7 MW/percentage of dispatchability). Regarding the CSP-only configurations, Table 12 explains the steep increment in LCOE observed in Figure 16 between 60% and 65% of satisfied demand: the cost increases because, to reach 65% dispatchability, it is necessary to install a considerably larger solar field (the SM increases from 4.0 to 6.5). Since no fossil fuel backup power has been considered, the only way the plant has to increase the energy produced is to exploit and collecting also the energy from low-irradiance hours but this results in a non-negligible increase in the size (and costs) of the solar-based components of the plant (SF and TES). Moreover, 65% dispatchability corresponds to the feasibility limit we found for this plant configuration (if we set higher levels of dispatchability, the optimizer cannot find a solution indicating that the CSP system cannot reach such targets). Finally, Table 12 shows that the hybrid solution corresponding to a 40% of annual satisfied demand collapse into the already found PV-BESS configuration, which is optimal for this dispatchability target. In the range 50-70% dispatchability the optimal plant is hybrid and it features the PV; PB, TES, SM and EH. The size and use of the EH increase with the dispatchability target. At 80%, s the optimal solution is quite unconventional since the solar field is not installed. All the heat required by the PB is generated by the excess PV electricity. Energy is stored as heat in the TES (8.7 h equivalent) and electricity in a 261 MWh BESS.

Table 12 - Optimal sizes of each plant component for different configurations and dispatchability levels

		Fraction of annual satisfied demand					
Configuration	**Sub-component**	**40%**	**50%**	**60%**	**65%**	**70%**	**80%**
PV-BESS	PV [MW_e]	111.8	149.7	160.3	171.5	186.2	257.0
	BESS [MWh]	38.0	115.4	236.7	290.8	341.5	416.5
CSP-only	PB [MW_e]	27.6	33.4	39.3	40.2	-	-
	TES [h]	11.9	12.6	13.5	14.3	-	-
	SM [-]	3.1	3.4	4.0	6.5	-	-
Hybrid no EH	PV [MW_e]	111.8	64.4	73.5	86.7	122.3	257.0
	BESS [MWh]	38.0	0.0	0.0	0.6	37.6	416.5
	PB [MW_e]	0.0	20.6	26.1	32.1	28.7	0.0
	TES [h]	0.0	13.1	13.7	11.6	13.7	0.0
	SM [-]	0.0	2.3	2.7	2.5	3.0	0.0
Hybrid	PV [MW_e]	111.8	87.8	108.2	120.7	172.3	257.0
	BESS [MWh]	38.0	0.0	0.0	0.0	0.0	261.6
	PB [MW_e]	0.0	21.0	21.5	27.0	30.5	20.6
	TES [h]	0.0	10.2	13.7	13.0	11.7	8.7
	SM [-]	0.0	1.4	2.0	1.7	1.0	0.0
	EH [MW_e]	0.0	21.9	35.3	44.7	76.8	70.0

Among the explored configurations, the hybrid system achieves the lowest cost of electricity in the whole dispatchability range considered. At 40% the hybrid configuration (both with and without EH) collapses to the PV-BESS solution which is the most economically advantageous for that value of the satisfied demand. The LCOE increase is limited until the x-axis value reaches 60%, then it starts sharply increasing as more expensive components (i.e. BESS) are necessary to met the remaining load share. However, remarkably, the hybrid plant can achieve a much better dispatchability level of the respective separated solutions (i.e. 80% against 65%) with a comparable cost of electricity (~ 232 €/MWh). The curve of the hybrid configuration in Figure 16 is very close to the one without EH. As the fraction of demand to be met increases, the difference between the two curves becomes large and the EH plays a key role to contain the LCOE. For the 80% of the annual demand met, the solution without the presence of EHs collapse to the PV-BESS configuration while the corresponding LCOE value of the hybrid plan with EH is 10% smaller (232 €/MWh vs. 257 €/MWh).

Finally, Figure 17 reports the LCOE and the value of the annual energy produced for the hybrid solution with EH considering demand fractions in the range 10-80%. The purpose of this figure is to show how the optimal plant design changes according to dispatchability level set as target. From the figure, four different regions can be identified:

- PV (green): for low dispatchability ranges (10-30%) the most convenient solution is the adoption of a PV field without storage, which allows to significantly contain the generation cost (LCOE < 70 €/MWh)
- PV-BESS (grey): for higher (medium-low) ranges of satisfied demand, the optimal configuration consists in the installation of a BESS other than the PV field. The battery presence avoids the excessive oversizing of the PV, reducing the quantity of energy curtailed. To cover at least 40% of the variable load, a system consisting of a PV of 111.8 MW and a storage of 38.7 MWh has been selected, featuring a LCOE of 125.5 €/MWh
- PV+CSP (yellow): for medium-high dispatchability levels (50-70%), the PV + BESS solution is progressively abandoned in favor of the hybrid PV + CSP system, which allows to further extend the flexibility range of the system without incurring in excessive costs (LCOE < 155 €/MWh). Going from the 50% to 60% of satisfied demand, both the size of the PV field and the CSP section (PB, TES, SF) are increased

- PV + CSP + BESS (blue): finally, when highly flexible and dispatchable systems are required (e.g. > 70%), the space allocated to the SF is progressively reduced while the installed capacity of PV increases. This trend is already visible in the solution at 70% that features a lower SM with respect to the previous one. At 80% dispatchability, the SF is not installed and the heat for the power block is provided by the excess PV.

Figure 17 - LCOE and yearly energy produced for different met demand fractions of the hybrid plant following a variable load

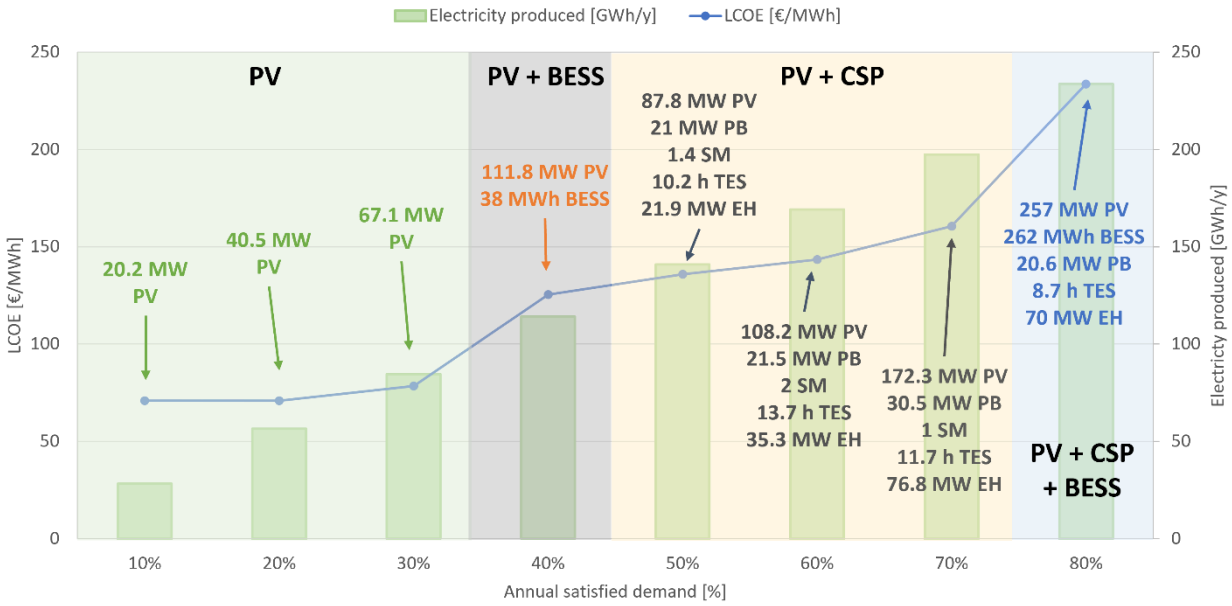

The solution reaching the maximum value of the demand fraction (80%) features an LCOE of 232 €/MWh and it is constituted by a 257 MW PV field, 262 MWh of BESS and a PB with a nominal power of 20.6 MW and a TES of 8.7 hours. The extensive utilization of the EH in this case is mainly motivated by (i) the lower cost of the system composed by the TES and the EH with respect to the BESS and to (ii) the specific production profile curve of the two solar technologies: while the thermal production of SF in two TPs (#5 and #6) is almost null, the PV generation is not completely zero in the same periods because its ability to capture part of the diffuse irradiance. Consequently, to cover the remaining fraction of demand in the less favorable days of the year, the optimization algorithm suggests to increase the installed power of the PV system rather than excessively oversize the SF.

7 Conclusion

This work establishes an innovative framework for the co-optimization of design and operation of hybrid CSP-PV power plants. All the system components have been characterized with ad-hoc models in several modeling environments, such SAM and Thermoflex. Then, the non-linear models have been linearized to fit the equation describing each subsystem inside a MILP formulation, representing the core of the optimization procedure. The optimization problem is able to find the optimal sizes of plant components and also derive its optimal dispatch over the optimization horizon, constituted by a set of typical periods accurately selected with a clustering algorithm.

To assess the potential benefits deriving from the technologies integration, the same methodology has been applied also to evaluate the optimal design and the performances of the two solar

technologies (CSP and PV-BESS), considered as stand-alone systems. A sensitivity analysis on the fraction of the annual load (i.e. dispatchability level) with the same hourly trend of the national electricity demand and a peak of 50 MW that the plant is able to fully cover has been done. The optimization outcomes demonstrated the convenience of the adoption of the hybrid plant layout for any of the explored dispatchability levels: hybrid solutions resulted in a lower cost of electricity (-35.3% and -47.7% with respect the CSP and PV-BESS, respectively) for the fraction of targeted demand (60%) and achieved a much reliable and more dispatchable design (covering 80% of the targeted load against 60% of stand-alone solutions) for a similar cost of electricity (232 €/MWh).

The analysis has investigated also the economic advantages of the physical hybridization (i.e., using an electric heater to convert the excess PV as useful heat for the thermal storage). With respect to a grid-integrated CSP-PV plant, using the electric heater allows reducing the cost of electricity by 3.6-10% depending on the target dispatchability (the higher the desired dispatchability, and the larger the advantage of using the electric heater). For the dispatchability level of 80%, maximum value reachable by the plants, the optimal design does not include the solar field: all the heat required by the power block derives from the excess electricity produced by the PV.

The results reported here have been obtained for an innovative medium-small scale CSP with Linear Fresnel Reflectors and molten salts, a plant suitable for particularly constrained locations such as densely populated EU countries. Large scale CSP plants might have better economic figures and the results of this paper cannot be directly extended. Another factor with important influence on the results might be the radiation profile (in particular the difference between DNI and GHI) of the installation site. For this reason, future works should repeat the analysis/optimization considering larger CSP scales, CSP technologies for the solar field and/or power block, and locations.

Acknowledgments

The results presented in this paper have been obtained in the framework of the “Concentrating Solar Power” project, under the “Electric System Research” program 2019–2021, with the financial support of Italian Ministry for Ecological Transition.

Appendix

In Figure 18 is reported the optimal operation strategy of the hybrid plant covering 60% of the variable annual demand. Figure 18a is shown the electricity produced and consumed by the plant for all the typical and extreme periods (separated by vertical black lines) while in Figure 18b is visible the corresponding management of the TES.

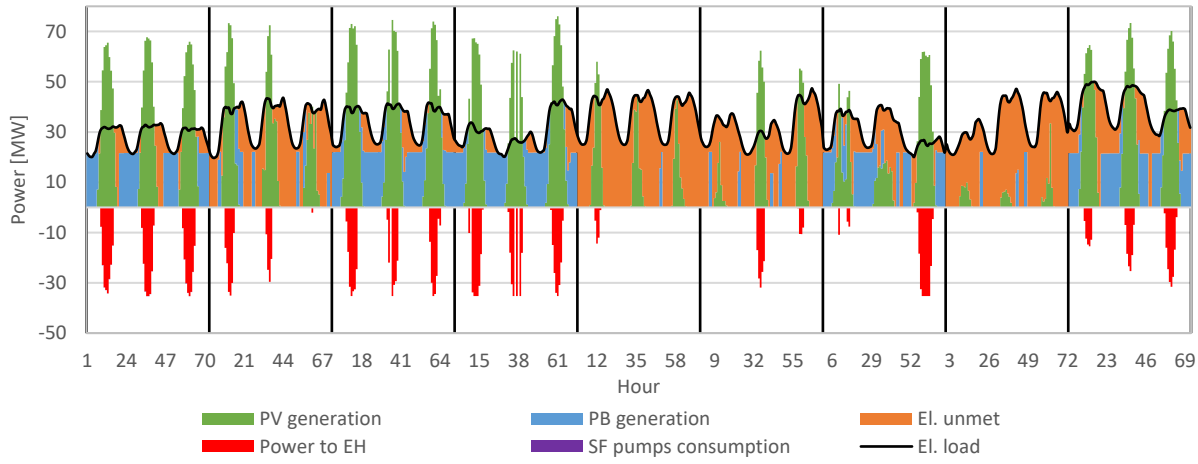

(a)

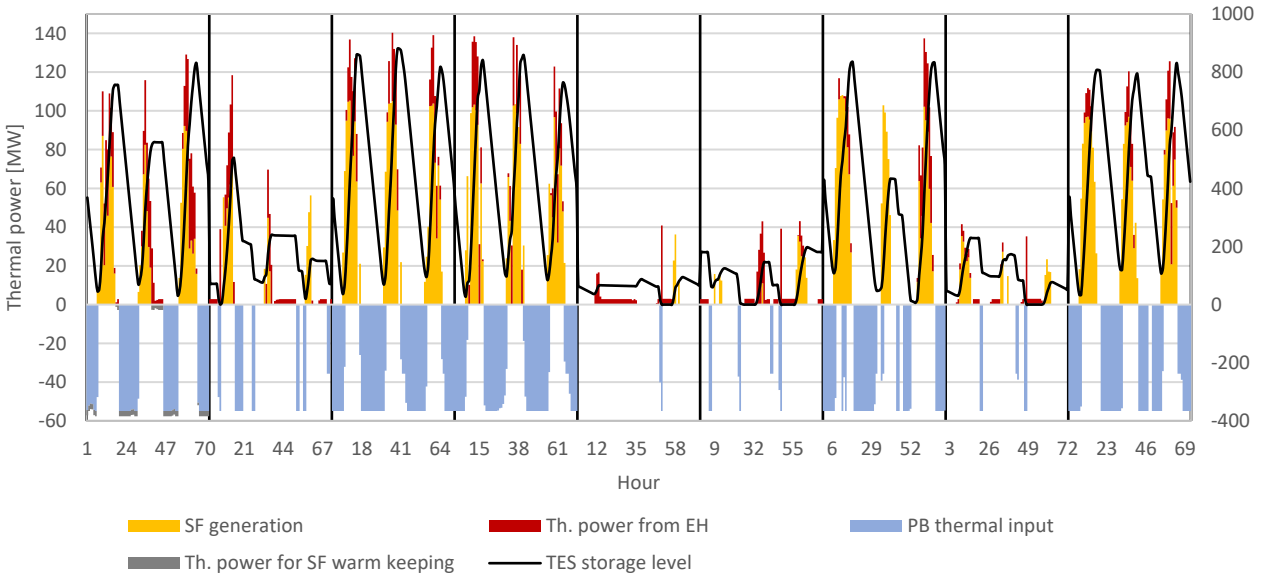

(b)

Figure 18 – Operation of the plant for each TP considered (separated by vertical black lines): electrical dispatch (a) and thermal management (b) of the TES.

Bibliography

[1] REN21, *Renewables 2020 Global Status Report*. 2020.

[2] W. Cole, A. W. Frazier, and C. Augustine, “Cost Projections for Utility-Scale Battery Storage: 2021 Update,” 2021. Accessed: Nov. 30, 2020. [Online]. Available: www.nrel.gov/publications.

[3] IRENA, *Renewable Power Generation Costs in 2020*. 2020.

[4] E. Martelli and L. Pilotti, “Integration of Renewable Energy Sources: A Review of Hybrid and Aggregated Energy Systems,” in *Renewable Energy*, AIP Publishing, 2022, p. 300.

[5] Z. Mahdi *et al.*, “Technical Assessment of Brayton Cycle Heat Pumps for the Integration in Hybrid PV-CSP Power Plants,” *SolarPACES*, 2020.

[6] Z. Mahdi *et al.*, “Modeling the thermal behavior of solar salt in electrical resistance heaters for

the application in PV-CSP hybrid power plants," *AIP Conf. Proc.*, vol. 2445, no. 1, p. 030013, May 2022, doi: 10.1063/5.0086268.

[7] J. M. Morales, A. J. Conejo, H. Madsen, P. Pinson, and M. Zugno, "Virtual power plants," in *International Series in Operations Research and Management Science*, vol. 205, Springer, Boston, MA, 2014, pp. 243–287.

[8] M. Petrollese, G. Cau, and D. Cocco, "The Ottana solar facility: dispatchable power from small-scale CSP plants based on ORC systems," *Renew. Energy*, vol. 147, pp. 2932–2943, Mar. 2020, doi: 10.1016/j.renene.2018.07.013.

[9] A. Mojiri, R. Taylor, E. Thomsen, and G. Rosengarten, "Spectral beam splitting for efficient conversion of solar energy—A review," *Renew. Sustain. Energy Rev.*, vol. 28, pp. 654–663, Dec. 2013, doi: 10.1016/J.RSER.2013.08.026.

[10] D. Cocco, L. Migliari, and M. Petrollese, "A hybrid CSP–CPV system for improving the dispatchability of solar power plants," *Energy Convers. Manag.*, vol. 114, pp. 312–323, Apr. 2016, doi: 10.1016/J.ENCONMAN.2016.02.015.

[11] A. R. Starke, J. M. Cardemil, R. Escobar, and S. Colle, "Multi-objective optimization of hybrid CSP+PV system using genetic algorithm," *Energy*, vol. 147, pp. 490–503, Mar. 2018, doi: 10.1016/j.energy.2017.12.116.

[12] "Ficha del Proyecto: 'PLANTA SOLAR CERRO DOMINADOR.'" https://seia.sea.gob.cl/expediente/ficha/fichaPrincipal.php?modo=ficha&id_expediente=2128879352 (accessed May 02, 2021).

[13] M. Falchetta *et al.*, "The Partanna Project: A first of a kind plant based on molten salts in LFR collectors," in *AIP Conference Proceedings*, Dec. 2020, vol. 2303, doi: 10.1063/5.0029269.

[14] K.-J. Riffelmann, G. Weinrebe, and M. Balz, "Hybrid CSP-PV Plants with Integrated Thermal Storage," 2020.

[15] Y. Gedle *et al.*, "Analysis of an integrated CSP-PV hybrid power plant," in *AIP Conference Proceedings*, 2022, vol. 2445, p. 030009, doi: 10.1063/5.0086236.

[16] X. Ju, C. Xu, Y. Hu, X. Han, G. Wei, and X. Du, "A review on the development of photovoltaic/concentrated solar power (PV-CSP) hybrid systems," *Sol. Energy Mater. Sol. Cells*, vol. 161, pp. 305–327, Mar. 2017, doi: 10.1016/j.solmat.2016.12.004.

[17] "Morocco Pioneers PV with Thermal Storage at 800 MW Midelt CSP Project - SolarPACES." https://www.solarpaces.org/morocco-pioneers-pv-to-thermal-storage-at-800-mw-midelt-csp-project/ (accessed Mar. 14, 2022).

[18] T. Crescenzi and M. Falchetta, *Opportunità di applicazione delle tecnologie solari in Italia*. 2016.

[19] O. P. Akkas and E. Cam, "Optimal Operation of Virtual Power Plant in a Day Ahead Market," in *2019 3rd International Symposium on Multidisciplinary Studies and Innovative Technologies (ISMSIT)*, Oct. 2019, pp. 1–4, doi: 10.1109/ISMSIT.2019.8932764.

[20] H. Saboori, M. Mohammadi, and R. Taghe, "Virtual power plant (VPP), definition, concept, components and types," *Asia-Pacific Power Energy Eng. Conf. APPEEC*, 2011, doi: 10.1109/APPEEC.2011.5749026.

[21] L. Heller, "Literature review on heat transfer fluids and thermal energy storage systems in CSP plants," *Lit. Rev. heat Transf. fluids Therm. energy storage Syst. CSP plants*, 2013, [Online]. Available: http://sterg.sun.ac.za/wp-content/uploads/2011/08/HTF_TESmed_Review_2013_05_311.pdf.

[22] A. Giostri, M. Binotti, P. Silva, E. Macchi, and G. Manzolini, "Comparison of two linear collectors in solar thermal plants: Parabolic trough vs fresnel," in *ASME 2011 5th International*

Conference on Energy Sustainability, ES 2011, Mar. 2011, no. PARTS A, B, AND C, pp. 621–630, doi: 10.1115/ES2011-54312.

[23] G. Morin, J. Dersch, W. Platzer, M. Eck, and A. Häberle, “Comparison of Linear Fresnel and Parabolic Trough Collector power plants,” *Sol. Energy*, vol. 86, no. 1, pp. 1–12, Jan. 2012, doi: 10.1016/J.SOLENER.2011.06.020.

[24] G. Morin, M. Karl, M. Mertins, and M. Selig, “Molten Salt as a Heat Transfer Fluid in a Linear Fresnel Collector – Commercial Application Backed by Demonstration,” *Energy Procedia*, vol. 69, pp. 689–698, May 2015, doi: 10.1016/J.EGYPRO.2015.03.079.

[25] “Download center - Terna spa.” https://www.terna.it/en/electric-system/transparency-report/download-center (accessed Jun. 10, 2022).

[26] SAM, “Home - System Advisor Model (SAM),” *NREL*, 2020. https://sam.nrel.gov/ (accessed Jun. 30, 2021).

[27] “THERMOFLEX - General Purpose Program - Heat Balance Software.” https://www.thermoflow.com/products_generalpurpose.html (accessed Jun. 17, 2021).

[28] “Solar Equipment List - CA Energy Commission.” https://solarequipment.energy.ca.gov/Home/Index (accessed Aug. 11, 2022).

[29] “Frenell - Startseite.” https://www.frenell.de/it/ (accessed Jun. 06, 2022).

[30] “Archimede Solar Energy.” http://www.archimedesolarenergy.it/it_hcems-11-sali-fusi.htm (accessed Jun. 17, 2021).

[31] “Archimede Solar Energy - Home.” http://www.archimedesolarenergy.it/.

[32] A. Giaconia, G. Iaquaniello, A. A. Metwally, G. Caputo, and I. Balog, “Experimental demonstration and analysis of a CSP plant with molten salt heat transfer fluid in parabolic troughs,” *Sol. Energy*, vol. 211, pp. 622–632, Nov. 2020, doi: 10.1016/J.SOLENER.2020.09.091.

[33] D. Belverato, E. Martelli, M. Binotti, L. Pilotti, and A. Giaconia, “Part-load of steam Rankine cycles for solar salts-based concentrating solar power plants,” 2022.

[34] E. Martelli, F. Alobaid, and C. Elsido, “Design Optimization and Dynamic Simulation of Steam Cycle Power Plants: A Review,” *Front. Energy Res.*, vol. 9, no. July, pp. 1–31, Jul. 2021, doi: 10.3389/fenrg.2021.676969.

[35] R. Yokoyama, Y. Hasegawa, and K. Ito, “A MILP decomposition approach to large scale optimization in structural design of energy supply systems,” *Energy Convers. Manag.*, vol. 43, no. 6, pp. 771–790, 2002, doi: 10.1016/S0196-8904(01)00075-9.

[36] M. Zatti, M. Gabba, M. Freschini, and E. Martelli, “The benefits of multi-energy systems optimization: The efficity project,” in *AIP Conference Proceedings*, Dec. 2019, vol. 2191, no. 1, p. 20009, doi: 10.1063/1.5138890.

[37] P. Gabrielli, M. Gazzani, E. Martelli, and M. Mazzotti, “Optimal design of multi-energy systems with seasonal storage,” *Appl. Energy*, vol. 219, no. May 2017, pp. 408–424, Jun. 2018, doi: 10.1016/j.apenergy.2017.07.142.

[38] F. Zaversky, J. García-Barberena, M. Sánchez, and D. Astrain, “Transient molten salt two-tank thermal storage modeling for CSP performance simulations,” *Sol. Energy*, vol. 93, pp. 294–311, Jul. 2013, doi: 10.1016/j.solener.2013.02.034.

[39] G. P. McCormick, “Computability of global solutions to factorable nonconvex programs: Part I - Convex underestimating problems,” *Math. Program.*, vol. 10, no. 1, pp. 147–175, Dec. 1976, doi: 10.1007/BF01580665.

[40] S. Giuliano, M. Puppe, and K. Noureldin, “Power-to-heat in CSP systems for capacity expansion,” *AIP Conf. Proc.*, vol. 2126, no. July, 2019, doi: 10.1063/1.5117589.

[41] C. S. Turchi *et al.*, “CSP Systems Analysis - Final Project,” *Nrel/TP-5500-72856*, no. May, 2019, [Online]. Available: www.nrel.gov/publications.

[42] M. Hoffmann, L. Kotzur, D. Stolten, and M. Robinius, “A review on time series aggregation methods for energy system models,” *Energies*, vol. 13, no. 3. p. 641, Feb. 03, 2020, doi: 10.3390/en13030641.

[43] M. Zatti *et al.*, “k-MILP: A novel clustering approach to select typical and extreme days for multi-energy systems design optimization,” *Energy*, vol. 181, pp. 1051–1063, 2019, doi: 10.1016/j.energy.2019.05.044.

[44] L. Kotzur, P. Markewitz, M. Robinius, and D. Stolten, “Impact of different time series aggregation methods on optimal energy system design,” *Renew. Energy*, vol. 117, pp. 474–487, Mar. 2018, doi: 10.1016/j.renene.2017.10.017.

[45] L. Taccari, E. Amaldi, E. Martelli, and A. Bischi, “Short-Term Planning of Cogeneration Power Plants: A Comparison Between MINLP and Piecewise-Linear MILP Formulations,” in *Computer Aided Chemical Engineering*, vol. 37, Elsevier B.V., 2015, pp. 2429–2434.

[46] L. Moretti, G. Manzolini, and E. Martelli, “MILP and MINLP models for the optimal scheduling of multi-energy systems accounting for delivery temperature of units, topology and non-isothermal mixing,” *Appl. Therm. Eng.*, vol. 184, p. 116161, Feb. 2021, doi: 10.1016/j.applthermaleng.2020.116161.

[47] Gurobi Optimization, LLC, “Gurobi Optimizer Reference Manual.” 2022, [Online]. Available: https://www.gurobi.com.

[48] “CPLEX Optimizer | IBM.” https://www.ibm.com/analytics/cplex-optimizer (accessed May 25, 2022).

[49] D. E. Hollermann, D. F. Hoffrogge, F. Mayer, M. Hennen, and A. Bardow, “Optimal (n−1)-reliable design of distributed energy supply systems,” *Comput. Chem. Eng.*, vol. 121, pp. 317–326, 2019, doi: 10.1016/j.compchemeng.2018.09.029.

[50] P. Marocco, D. Ferrero, E. Martelli, M. Santarelli, and A. Lanzini, “An MILP approach for the optimal design of renewable battery-hydrogen energy systems for off-grid insular communities,” *Energy Convers. Manag.*, vol. 245, p. 114564, Oct. 2021, doi: 10.1016/j.enconman.2021.114564.

[51] K. Mongird *et al.*, “Energy Storage Technology and Cost Characterization Report,” 2019.

[52] G. Cardoso, T. Brouhard, N. DeForest, D. Wang, M. Heleno, and L. Kotzur, “Battery aging in multi-energy microgrid design using mixed integer linear programming,” *Appl. Energy*, vol. 231, no. December, pp. 1059–1069, 2018, doi: 10.1016/j.apenergy.2018.09.185.

[53] W. Short, D. Packey, and T. Holt, “A manual for the economic evaluation of energy efficiency and renewable energy technologies,” *Renew. Energy*, vol. 95, no. March, pp. 73–81, 1995, doi: NREL/TP-462-5173.